Journal of Sound and Vibration 621 (2026) 119433

Contents lists available at ScienceDirect

Journal of Sound and Vibration

journal homepage: www.elsevier.com/locate/jsvi

Multi-tortuous acoustic materials

Tomasz G. Zieliński [a,*], Marie-Annick Galland [b]

[a] Institute of Fundamental Technological Research, Polish Academy of Sciences, ul. Pawińskiego 5B, 02-106 Warsaw, Poland
[b] Ecole Centrale de Lyon, CNRS, UCB Lyon 1, INSA Lyon, LMFA, UMR 5509, Ecully, France

ARTICLE INFO

Keywords:
Multi-resonant acoustic materials
Disconnected pore networks
Multi-pressure model
Tortuosity-based design
Sound absorption

ABSTRACT

In this work, a multi-pressure equivalent fluid (MPEF) approach is applied to model non-conventional acoustic materials that combine different, separate pore networks with contrasting tortuosities. A technique for the informed design of such *multi-tortuous* materials is proposed. It is based on the observation that broadband performance of such a material can be achieved by tuning the quarter-wavelength resonances corresponding to each network. The material design consists therefore in adding and tailoring the separate pore networks to obtain contrasting tortuosities that evenly distribute these resonances over the desired frequency range. Additional improvement is achieved by independent isotropic scaling of the separate networks. The proposed technique is accurate and also very efficient because it is based on semi-analytical calculations. All this is demonstrated on several examples of multi-tortuous materials which, for simplicity, have an essentially two-dimensional structure. The results obtained in the material design process are verified by Navier–Stokes direct numerical simulations as well as by the MPEF numerical model. Final validation was also carried out experimentally on an additively manufactured sample of one of the multi-tortuous materials designed for this study. The multi-resonance phenomenon observed in sound absorption as well as the experimentally demonstrated anomalous behaviour of the multi-tortuous material backed by an air gap are very well predicted by the modelling and explained in detail on physical grounds.

1. Introduction

It is well-known that traditional acoustic treatments such as porous materials do not provide good low-frequency performance when their thickness is limited [1]. However, control of low-frequency noise is often required in practical situations, while at the same time, restrictions are imposed on the volume and weight of the sound insulating or absorbing material. When the noise source is well known and tonal in nature, efficient acoustic solutions based on the resonance behaviour of engineered acoustic structures or panels can be designed. This is because the designs can be tuned to a known frequency. However, conventional resonance-based solutions such as micro-perforated plates (MPP) backed by air cavities and Helmholtz resonators in their classical form are bulky when tuned to a low frequency and exhibit narrowband behaviour around the resonance. To reduce the structure thickness, various architected materials and metamaterial solutions [2] have been proposed and investigated in recent years. The goal is sub-wavelength performance, which means that the thickness of the acoustic material is much smaller than the wavelength of the acoustic wave it attenuates; the wavelength is defined in air, i.e. before the wave penetrates the material. Cai et al. [3] proposed a sub-wavelength metamaterial solution in the form of thin acoustic panels with coiled coplanar tubes or chambers. Solutions based on similar ideas include: coiled cavities [4,5], coiled Helmholtz resonators [6], labyrinthine channels [7–10], and folded

* Corresponding author.
E-mail address: tzielins@ippt.pan.pl (T.G. Zieliński).

https://doi.org/10.1016/j.jsv.2025.119433
Received 9 April 2025; Received in revised form 15 July 2025; Accepted 28 August 2025
Available online 4 September 2025

quarter-wavelength resonators [11]. Catapane et al. [12] showed that coiled quarter-wavelength resonators for low-frequency sound absorption are also efficient in diffuse acoustic field. Ramos et al. investigated low-frequency acoustic metastructures composed of critically coupled sub-wavelength Helmholtz resonators at different incidence angles [13] and under grazing incidence [14].

The narrowband problem can be to some extent alleviated with double-porosity solutions [10]. This approach can be combined with multi-resonant solutions, which are most suitable to overcome the problem of narrowband performance at low frequencies. Such solutions consist in combining different acoustic materials or structures that are effective in complementary frequency ranges because their own resonances (due to quarter-wavelength, membrane or Helmholtz resonators) are different. This idea was implemented by Sakagami et al. [15,16] in the form of a parallel combination of two MPPs backed by air cavities. MPP absorbers are well-known acoustic solutions that can be tuned to a specific frequency range by changing the cavity depth behind the MPP, while the perforation size and rate can be optimised to achieve perfect peak absorption [17]. Therefore, broadband sound absorption can obtained with periodically repeated systems of several MPP absorbers arranged in parallel and having different cavity depths [18]. The cavity depths should be adjusted for complementary performances. In their seminal work, Verdière et al. [19] applied the transfer matrix method (TMM) to the parallel assembly of sound absorbing materials. The method is very useful to study sound absorption and transmission by layers of heterogeneous materials such as patchworks, acoustic mosaics, or a collection of acoustic elements in parallel.

In recent years, research on multi-resonant techniques and designs for enhanced acoustic treatments has been intensified. Many of these combine the concepts of MPP absorbers and coiled cavities or other solutions. For example, a parallel arrangement of three perforated plates with extended tubes, open-cell foam and MPP was studied by Li et al. [20]. Elastic MPPs in parallel arrangement were investigated by Hyun et al. [21]. Almeida et al. [22] proposed an acoustic metamaterial based on MPP coupled to a multi-cavity of coiled-up spaces that is similar to a symmetrical labyrinth. Recent similar examples include: a composite sound absorber composed of MPPs backed by impedance-matching nesting channels partly filled with a porous material [23], an MPP supported by four U-shaped cavities with different depths arranged in parallel [24], an MPP absorber with parallel optimised coiled-up-cavities of different-depths [25]. In general, sub-wavelength multi-resonant behaviour can be obtained by various acoustic metamaterials such as arrays of Helmholtz resonators and air cavities, membrane or elastic-plate resonators [2]. Representative examples are: parallel assemblies of coiled-up resonators [26] or spiral cavities [27], nested or parallel arrangements of Helmholtz resonators [13,28,29]. Recent works on broadband, multi-resonant materials and metamaterials also deal with problems and configurations other than normal incidence sound absorption; this includes: transmission problems in wide waveguides [30], sound attenuation in ducts using nested-network liners under grazing incidence [31], sound attenuation in ducts with grazing flow [32–34]. A significant improvement in sound absorption is observed in the case of multi-resonant lateral cavities such a various dead-end pores located along the main pore [35] or slits of various length distributed along the profile of an acoustic black hole [36,37].

In this paper, the concept of multi-tortuous acoustic materials with multiple, disconnected open-pore networks is presented, along with a full theoretical discussion on the modelling of such materials. In contrast to conventional acoustic approaches usually applied for materials with curved channels and coiled-up cavities (see relevant references cited above), a much more versatile and highly accurate multi-pressure approach based on dissipative equivalent fluids is proposed that allows modelling materials with multiple open-pore networks of virtually *any* geometry. The unusual acoustic behaviour of such materials, observed when the material layer is supported by an air gap, is thoroughly explained on the basis of the developed theory. Based on this modelling, an original and effective design method has been developed to combine optimised networks with tuned, contrasting tortuosities, ensuring broadband sound attenuation by such a multi-tortuous material. This is achieved due to multi-resonant behaviour resulting from different quarter-wavelength resonances distributed (by design) over the desired low-frequency range. The multi-pressure model for such materials is introduced in Section 2, starting from the classical theory of porous materials with a rigid frame. An original technique for the informed semi-analytical design of multi-tortuous materials is discussed in detail in Section 3, using several examples. Section 4 presents an experimental validation of the theory based on a 3D printed sample of one of the designed materials, along with additional numerical verification. The specific and unusual acoustic behaviours of multi-tortuous materials are also discussed in this section. The main findings and conclusions are summarised in Section 5.

2. Mathematical modelling

2.1. Porous materials with a single pore network

2.1.1. Equivalent-fluid modelling

Let us first consider a porous material with a rigid frame and a single open-pore network denoted by n, see Fig. 1(a). In such a compact (single) network of pores, all pores are open, interconnected and fully saturated with air. It is important to note, however, that generally speaking, n can denote a group of identical networks, because the equivalent-fluid modelling discussed here also applies to the special case where the material contains a periodic arrangement of separate but *identical* open-pore networks, channels or slits – as illustrated by the example shown in Fig. 1(b) – in which the wave propagation is the same. The pore networks of real porous materials often have a very regular geometry that can be represented by a periodic element called a unit cell or a representative elementary volume, while designed 3D printed materials are usually built on such a periodic cell. The unit cell contains all the information about the pore network geometry, see Fig. 1, and its intrinsic parameters, including the porosity ϕ_n, characteristic dimensions, tortuosity, permeability, etc. The periodicity enables the application of rigorous homogenisation techniques such as two-scale asymptotic method [38,39] to model acoustic wave propagation in such materials provided that the wavelengths are much larger than the unit cell size. The final results of this homogenisation are briefly discussed

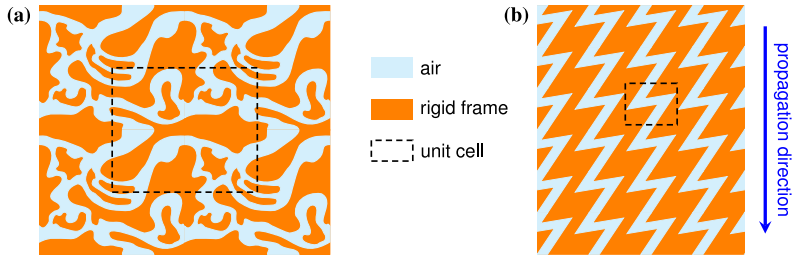

Fig. 1. Porous and slotted materials (with a single tortuosity): (a) a rigid-frame porous material with a periodic open-pore network, (b) a rigid-frame slotted material with a periodic arrangement of identical zigzag-shaped slits.

below. The main outcome is that the porous or slotted material is replaced with a homogeneous lossy medium of an equivalent fluid (EF) with frequency-dependent and complex-valued properties that take into account dispersion and visco-thermal dissipation effects occurring at the micro-scale, i.e. inside the unit cell. The two independent effective properties of the EF are the effective density and the effective speed of sound (see below). They both depend on the dynamic viscous permeability of the porous material, which is generally a second-order tensor. However, many porous materials can be treated as isotropic when their viscous permeability is a quasi-spherical tensor that can be replaced by its trace. In other cases, and particularly in this work, the analysed wave propagation is often in a specific, i.e. known, direction. Then, the permeability tensor can be replaced by its (double) projection onto the direction of wave propagation, see Fig. 1(b). As a result, both the effective density and the effective speed of sound are scalars, or rather, complex-valued scalar functions of frequency, and the EF is isotropic.

Airborne acoustic waves that penetrate open-porosity materials such as those depicted in Fig. 1 cause oscillatory flow in the pores. Let $p^{(n)}$ and $\mathbf{v}^{(n)}$ denote the average pressure and velocity in the pores, respectively, or rather the frequency-dependent complex amplitudes of these state variables, as the wave propagation is described assuming a Fourier time convention of the type $\exp(+\mathrm{i}\omega t)$. Here, t is time, $\omega = 2\pi f$ is the angular frequency, f is the 'ordinary' frequency, and $\mathrm{i} = \sqrt{-1}$. In the following, it is convenient to use the volumetric flux $\mathbf{V}^{(n)} = \phi_n \mathbf{v}^{(n)}$, i.e. the rate of volume flow across a unit area of a porous material. This flux is related to the pressure gradient in two ways [39,40], namely

$$\mathbf{V}^{(n)} = -\frac{\nabla p^{(n)}}{\mathrm{i}\omega \varrho_n(\omega)} = -\frac{\mathcal{K}_n(\omega)}{\eta_\mathrm{a}} \nabla p^{(n)}\,, \tag{1}$$

where ϱ_n and $\mathcal{K}_n$ are the effective density and dynamic viscous permeability of the porous material, respectively, whereas η_a is the dynamic viscosity of air. The first relationship follows from the linearised momentum equation, while the second is a dynamic generalisation of Darcy's law [39–41]. The two relations (1) link the effective density with the dynamic permeability. Along with the effective compressibility C_n, the two fundamental effective properties of an air-saturated porous material are derived as follows

$$\varrho_n(\omega) = \frac{\eta_\mathrm{a}}{\mathrm{i}\omega \mathcal{K}_n(\omega)}\,, \qquad C_n(\omega) = \frac{\phi_n}{P_0}\left(1 - \frac{\Theta_n(\omega)}{\phi_n}\frac{(\gamma_\mathrm{a}-1)}{\gamma_\mathrm{a}}\frac{\mathrm{i}\omega}{\tau_\mathrm{a}}\right). \tag{2}$$

Here, P_0 is the ambient mean pressure, γ_a is the adiabatic index of air, and τ_a is the thermal diffusivity of air, while Θ_n is the dynamic thermal permeability of the porous material. Homogenisation by the multiscale asymptotic method [38,39] assumes that the viscous and thermal effects are uncoupled at the microscale, i.e. inside the pores, which means the two dynamic permeabilities, $\mathcal{K}_n$ and Θ_n, can be determined independently.

Assuming elastic behaviour and therefore an elastic constitutive relation for the equivalent fluid, the mass continuity equation for a porous medium with pore network n takes the following form

$$\nabla \cdot \mathbf{V}^{(n)} + \mathrm{i}\omega\, C_n(\omega)\, p^{(n)} = 0\,. \tag{3}$$

Combining the continuity and momentum equations for oscillatory viscous flow through the pore network n saturated with air, i.e. Eq. (3) with the first relationship of Eqs. (1), leads to the classic Helmholtz equation

$$\nabla^2 p^{(n)} + k_n^2(\omega)\, p^{(n)} = 0 \tag{4}$$

that describes the propagation of acoustic waves in an equivalent fluid replacing the porous medium. Here, the complex wave number k_n, together with the effective speed of sound c_n, and the effective characteristic impedance Z_n, are calculated for the porous material using its fundamental effective properties (2) as follows

$$c_n(\omega) = \Big(\varrho_n(\omega)\, C_n(\omega)\Big)^{-1/2}, \qquad k_n(\omega) = \frac{\omega}{c_n(\omega)}\,, \qquad Z_n(\omega) = \varrho_n(\omega) c_n(\omega)\,. \tag{5}$$

After the effective properties are determined, wave propagation in a porous material can be studied by solving a boundary value problem of the Helmholtz equation (4) defined in the region of the effective acoustic fluid, which is equivalent to the porous

material. In general, this requires numerical calculations, but analytical solutions are available, e.g. for plane wave propagation. In the case of porous materials or multi-layered systems that include such materials, these solutions form the basis for the transfer matrix method (TMM) [1,42] and are often used to determine useful acoustic indicators and even the effective fluid properties [43]. One of these indicators is the surface acoustic impedance defined at a given surface as the ratio of the sound pressure at that surface to the acoustic particle velocity or its porous-medium equivalent, the volumetric flux. It is an important acoustic property because, among other things, it can be used to determine other acoustic indicators such as reflection and sound absorption coefficients [1], see Appendix A.

2.1.2. Surface acoustic impedance and the transfer matrix method

Let us consider plane wave propagation along the x-axis in the direction of the unit vector $\mathbf{x}$, see Fig. 2(a). The surface acoustic impedance $\mathcal{Z}_\mathrm{S}$ at point $x = x_0$ can be determined knowing the surface impedance at point $x = x_0 + \ell$, namely

$$\mathcal{Z}_\mathrm{S}(x_0) = \frac{p(x_0)}{\pm\mathbf{v}(x_0)\cdot\mathbf{n}} = \frac{p(x_0)}{\mathbf{v}(x_0)\cdot\mathbf{x}} = \frac{T_{11} + T_{12}/\mathcal{Z}_\mathrm{S}(x_0+\ell)}{T_{21} + T_{22}/\mathcal{Z}_\mathrm{S}(x_0+\ell)}, \tag{6}$$

where T_{11}, T_{12}, T_{21} and T_{22} are the components of the transfer matrix $\mathbf{T}$ defining the relationship between acoustic pressure and velocity at two points. In the definition (6), p and $\mathbf{v}$ are the sound pressure and acoustic particle velocity, respectively. The latter can be formally replaced by the volumetric flux if the point $x = x_0$ lies inside a porous medium, see Fig. 2(b). Furthermore, ℓ is the distance between the two parallel surfaces, $\mathbf{n}$ is the unit vector normal to the surface, and the sign $\pm = \mathbf{x}\cdot\mathbf{n}$ (note that the unit vectors $\mathbf{x}$ and $\mathbf{n}$ are collinear, but can have any orientation; in any case: $\pm\mathbf{v}\cdot\mathbf{n} = \mathbf{v}\cdot\mathbf{x}$).

The transfer matrix $\mathbf{T}$ depends of the material properties and the distance ℓ. In particular, $\mathbf{T} = \mathbf{T}^{(n)}(\ell)$ for a homogeneous layer with a pore network n, where

$$\mathbf{T}^{(n)}(\ell) = \begin{bmatrix} T_{11}^{(n)}(\ell) & T_{12}^{(n)}(\ell) \\ T_{21}^{(n)}(\ell) & T_{22}^{(n)}(\ell) \end{bmatrix} = \begin{bmatrix} \cos(k_n\ell) & \mathrm{i}\sin(k_n\ell)Z_n \\ \mathrm{i}\sin(k_n\ell)/Z_n & \cos(k_n\ell) \end{bmatrix}. \tag{7}$$

Note that $\det\mathbf{T}^{(n)} = T_{11}^{(n)}T_{22}^{(n)} - T_{12}^{(n)}T_{21}^{(n)} = 1$, which means that the material is reciprocal. An impervious, rigid wall at $x = x_0+\ell$ means that $\mathcal{Z}_\mathrm{S}(x_0+\ell) \to \infty$, and in this case $\mathcal{Z}_\mathrm{S}(x_0) = T_{11}/T_{21}$. In particular, for a homogeneous porous layer with thickness H set on a rigid wall, see Fig. 2(c), $\mathcal{Z}_\mathrm{S} = \mathcal{Z}_\mathrm{S}^{(n)}(H)$, where

$$\mathcal{Z}_\mathrm{S}^{(n)}(H) = \frac{T_{11}^{(n)}(H)}{T_{21}^{(n)}(H)} = Z_n\coth\left(\mathrm{i}k_nH\right) \tag{8}$$

is the surface impedance for such a layer with a pore network n, characterised by the wave number k_n and the characteristic impedance Z_n. For a multi-layer system set on a rigid wall, the formula $\mathcal{Z}_\mathrm{S} = T_{11}/T_{21}$ holds, but the transfer matrix $\mathbf{T}$ is the product of the transfer matrices for all subsequent layers. In particular, $\mathbf{T} = \mathbf{T}^{(n)}(H)\,\mathbf{T}^{(\mathrm{a})}(H_\mathrm{g})$ for a two-layer system of a porous material with thickness H backed by an air gap with thickness H_g, see Fig. 2(d). Here, $\mathbf{T}^{(\mathrm{a})}(H_\mathrm{g})$ is the transfer matrix for the air gap, defined

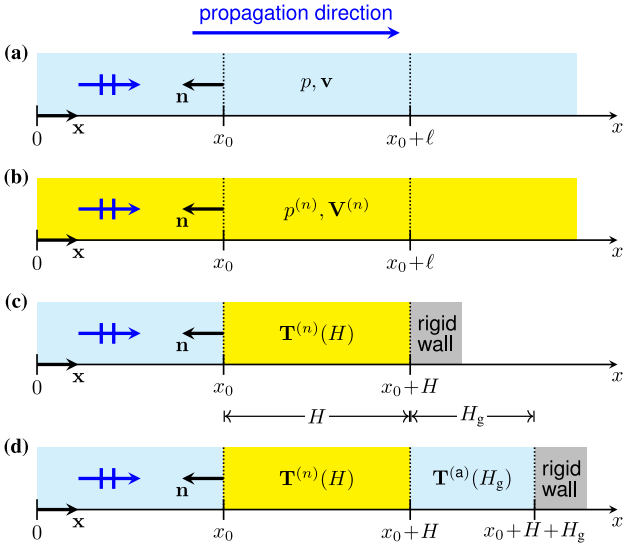

Fig. 2. Plane wave propagation in homogeneous media such as (a) air, or (b) isotropic fluids equivalent to air-saturated porous materials, and (c,d) multilayer systems of such materials – for analysis by the transfer matrix method.

by Eq. (7) after substituting $n = \mathrm{a}$ and $\ell = H_\mathrm{g}$, assuming that $k_\mathrm{a} = \omega/c_\mathrm{a}$ and $Z_\mathrm{a} = \varrho_\mathrm{a} c_\mathrm{a}$ are the wave number and characteristic impedance of air, respectively, where c_a is the speed of sound and ϱ_a is the density of air. Alternatively, the surface impedance $\mathcal{Z}_\mathrm{S}$ for a porous layer backed by an air gap can be calculated using Eq. (6) with $\mathbf{T} = \mathbf{T}^{(n)}(H)$ and $\mathcal{Z}_\mathrm{S}(x_0 + \ell) = \mathcal{Z}_\mathrm{S}^{(\mathrm{a})}(H_\mathrm{g})$, where the surface impedance of the air gap itself is $\mathcal{Z}_\mathrm{S}^{(\mathrm{a})}(H_\mathrm{g}) = T_{11}^{(\mathrm{a})}(H_\mathrm{g})/T_{21}^{(\mathrm{a})}(H_\mathrm{g}) = Z_\mathrm{a}\coth\left(\mathrm{i}k_\mathrm{a}H_\mathrm{g}\right)$, cf. Eq. (8).

2.2. Materials with multiple, i.e. disconnected open-pore networks

2.2.1. Multi-pressure equivalent fluid model

Let us consider a rigid-frame porous material with different open-pore networks saturated with air. Fig. 3(a) shows a two-dimensional example with $N = 3$ periodic arrangements (groups) of separate networks. The networks from each group are identical, and in the case of three-dimensional geometries, they could be interconnected creating one periodic network that is separated from the other two periodic networks. Therefore, the networks from each group are collectively assigned a unique successive integer $n = 1, \ldots, N$. The material may have multiple periodicity, but one can usually define a collective unit cell – see the dashed rectangle in Fig. 3(a) – that is fully representative for the entire material. To simplify further discussions, we assume that such a collective unit cell contains only one network from each group, as exemplified in Fig. 3(a). Note that in the case of three-dimensional geometries, different pore networks can share the representative elementary volume of the material in a more sophisticated way than that shown in Fig. 3(a). For example, one network can be nested within another (like a channel inside a channel), provided that their air domains are separated from each other.

Each network from a given group n is fully representative for the entire group and for the sake of simplicity we will rather talk about the network n even if, more precisely, it is about the entire network group (recall that in 3D a network group can be just one compact periodic network). The network n is characterised by its intrinsic parameters and properties as indicated in Section 2.1. In particular, the porosity ϕ_n is the volume fraction of network n with respect to the total volume of the entire collective unit cell, i.e. including the volumes of other networks. However, the standard EF modelling cannot generally be applied to materials with different open-pore networks, i.e. when $N > 1$. This is because the pore region inside the unit cell is not compact but it consists of different, disconnected networks in which the wave propagation is locally independent and therefore can be fundamentally different. This means in particular that the pressures in networks inside the collective representative unit cell may differ in phase and cannot be cumulatively replaced by a single averaged macroscopic pressure. This happens especially when the propagation speeds associated with each of the pore networks are significantly different. We will show in Section 3 that for networks with higher tortuosities (and larger viscous characteristic lengths) those speeds depend primarily on the tortuosity and significant change in tortuosity results in a completely different propagation speed. When the separated open-pore networks have identical or very similar tortuosity and characteristic lengths, an approach based on one pressure variable, i.e. using a single EF, may be applied as a first approximation. However, this single-pressure approach fails in the case of the multi-tortuous materials studied in this work.

Fig. 3(e) shows a simple, generic example of a configuration with a layer of porous material with N separated open-pore networks. Note that it may be a (periodic) fragment of a larger configuration containing this material. The porous layer is mounted on a rigid wall that has an irregular air-saturated cavity which is covered from above with the layer, see also Fig. 3(d). We assume that on the left side of the cavity, the layer is glued to the wall, so the pore networks are perfectly sealed on this side, see Fig. 3(b). In contrast to this, on the right side of the air cavity, the layer is simply placed loosely on the wall so that an infinitely thin air gap is created between them as illustrated in Fig. 3(c). In the case of porous materials with different, i.e. separated, open-pore networks, this subtle difference leads to different boundary conditions and ultimately results in fundamentally different wave propagation. The hard boundary condition with an infinitely thin air gap naturally transforms into an interface coupling condition when the air gap is not infinitely thin, as in the case of air cavity shown in Fig. 3(d). Generally speaking, the interface coupling condition applies at the edge of the material, where it meets an air domain (or an EF domain).

We propose a multi-pressure equivalent fluid (MPEF) model to analyse the propagation of sound waves in a material with N disconnected pore networks, in configurations with boundary and interface conditions like those described above. This homogenised model is composed from N effective fluids that independently occupy the same domain of the material, as illustrated by the diagram shown in Fig. 3(f) for the case when $N = 3$. The EF denoted by n is acoustically equivalent to the corresponding porous material with a single network n that can be represented by the corresponding unit cell – see Cell 1, 2 and 3 in Fig. 3(f) – and as such it is characterised in particular by the wave number k_n and the characteristic impedance Z_n. As a consequence, in the same computational domain of the material,[1] N independent Helmholtz equations are defined for all equivalent fluids, each for a different acoustic pressure $p^{(n)}$. The Helmholtz equations are not coupled inside the computational domain. However, they are coupled at the interfaces with air domains or other acoustic media (e.g. conventional porous acoustic materials), as well as on some boundaries, excluding the perfectly sealed ones or planes of symmetry, as discussed below. In other words, although sound waves propagating in the equivalent fluids do not interact within the material domain, their propagation is not independent due to interactions at its boundaries. Therefore, to analyse this propagation, one needs to solve the coupled multi-pressure system of N Helmholtz equations (possibly plus additional Helmholtz – or other – equations defined in adjacent domains).

To simplify the notation below, we assume that summing over n means summation over the entire set of N pore networks, i.e. $\sum_n(\ldots) \equiv \sum_{n=1}^{N}(\ldots)$. Thus, for example, the total porosity of the material equals $\sum_n \phi_n$, while $\sum_n \mathbf{V}^{(n)}$ is the total volumetric flux, i.e. the sum of fluxes coming from all networks.

[1] Alternatively, we can also talk about N computational domains that completely overlap, i.e. occupy the same geometric space. This is because in the case of finite element calculations, a different finite element mesh could possibly be used for each of them, although this would rather be impractical.

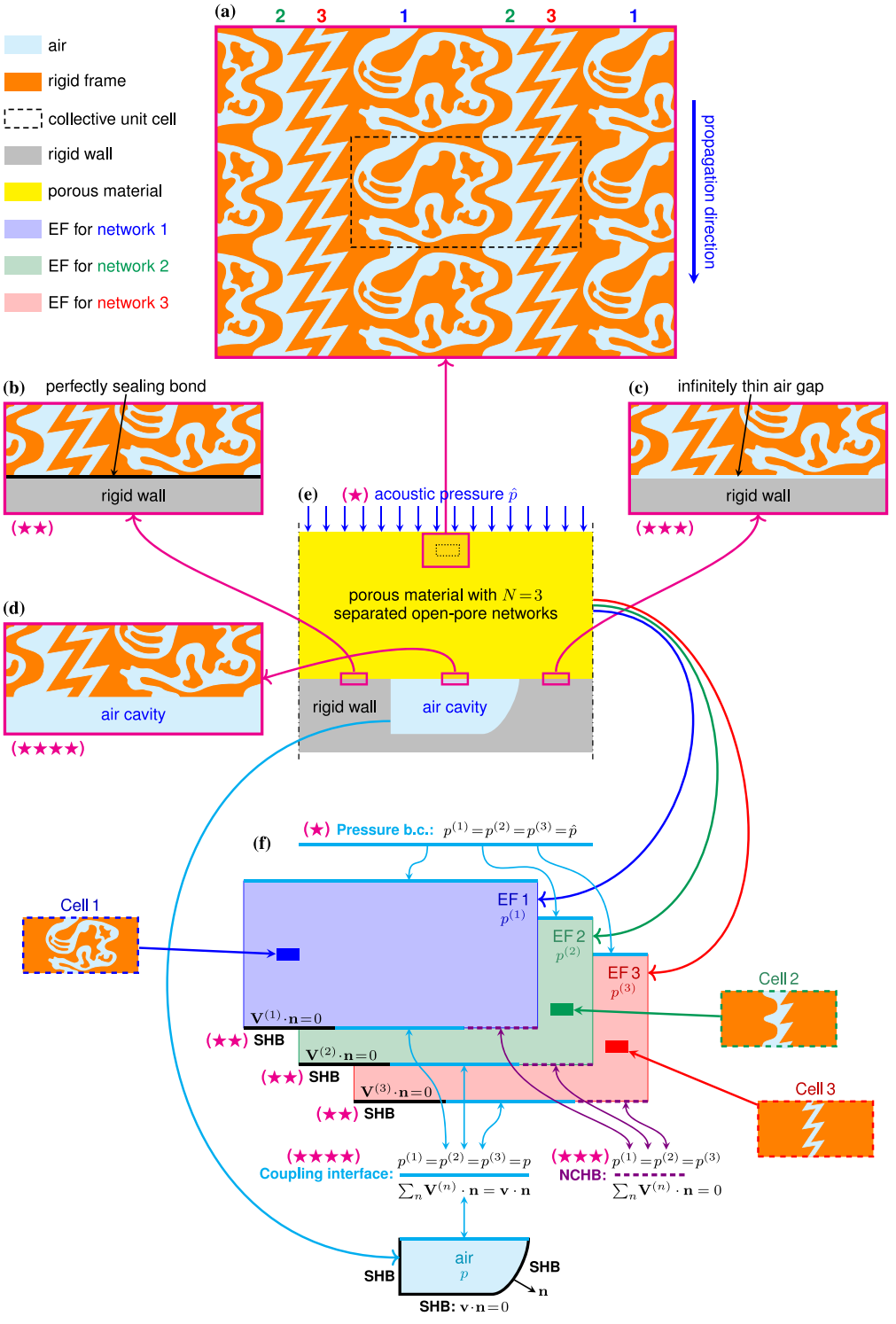

Fig. 3. Material with $N = 3$ separated open-pore networks in a configuration with various boundary and interface conditions: (a) the microstructure of the multi-network material, (b,c,d) different boundary and interface conditions, (e) the macroscopic configuration, and (f) the corresponding MPEF model.

2.2.2. Interface coupling and boundary conditions

The MPEF model is distinguished from other models that include the Helmholtz equations defined in different domains by specific interface coupling and boundary conditions. Coupling conditions at the MPEF interface with the air domain, see Fig. 3(d), ensure the continuity of acoustic pressure and velocity in the following way

$$\forall n \quad p^{(n)} = p\,, \qquad \sum_n \mathbf{V}^{(n)} \cdot \mathbf{n} = \mathbf{v} \cdot \mathbf{n}\,. \tag{9}$$

Such a coupling interface is marked with four asterisks on the MPEF model diagram shown in Fig. 3(f). Here, p and $\mathbf{v}$ are the acoustic pressure and particle velocity in the adjacent air domain, and $\mathbf{n}$ is the unit vector normal to the interface. Note that these are $(N+1)$ conditions, i.e. N conditions for pressure variables and one condition for the total flux. It should also be noted that the pressures of all networks equalise at the interface. In the case where the adjacent domain is an air-saturated porous material (instead of air), p and $\mathbf{v}$ in Eqs. (9) are replaced by the corresponding pore pressure and velocity flux.

Dirichlet boundary conditions can be used to simulate the effect of airborne acoustic waves impinging at normal incidence on the surface of the material, see the boundary marked with one asterisk in Fig. 3(e,f). In the case of a material with N disconnected pore networks, this is realised by the following N equations

$$\forall n \quad p^{(n)} = \hat{p}\,. \tag{10}$$

Here, the acoustic pressures coming from all pore networks are coupled on the boundary, as they are equalised by the applied pressure $\hat{p}$.

Neumann boundary conditions are used to apply a known velocity $\hat{v}$, perpendicular to the boundary of the material domain. In particular, when a porous material is placed on a rigid wall: $\hat{v} = 0$, which is the well-known condition of sound-hard boundary (SHB). This condition applies to the volumetric flux at a rigidly supported boundary of a single-network material. However, for materials with multiple disconnected networks, two fundamentally different cases need to be considered. Firstly, if we suppose that all pore networks are sealed by the wall, as shown in Fig. 3(b), the flux of *each* network is zeroed at this boundary, i.e.

$$\forall n \quad \mathbf{V}^{(n)} \cdot \mathbf{n} = 0\,. \tag{11}$$

As a consequence, the pore network pressures remain independent on each other. Eqs. (11) define N homogeneous Neumann-type conditions for a *perfectly sealed* SHB. In Fig. 3(f), all SHB conditions are marked with two asterisks. It should be noted that such conditions must also be applied in the case of a symmetry plane, because planes of symmetry occur inside the material, i.e. where the pore networks are separated. On the other hand, in practical situations, when a porous material is placed on a rigid wall, without being glued to it or pressed hard against it, an extremely thin layer of air may often remain between the wall and the material. For single-network porous materials, this leakage is usually negligible, since what we have is an infinitely thin air gap. However, the situation becomes more dramatic in the case of a porous material with multiple disconnected networks: the thin air layer – even an infinitely thin one – connects the substantially different pore networks, as depicted in Fig. 3(c), and thus equalises their pressures. We will call this case a *network-coupling hard boundary* (NCHB). It is fundamentally different from the perfectly sealed SHB condition. NCHB is marked with three asterisks in Fig. 3(f) and described by the following N boundary conditions

$$p^{(1)} = \cdots = p^{(N)}\,, \qquad \sum_n \mathbf{V}^{(n)} \cdot \mathbf{n} = 0\,, \tag{12}$$

which equalise the pressures and zero the total velocity flux. Note that for $N = 1$, i.e. for a single network, Eqs. (12) and (11) reduce to the same SHB condition: $\mathbf{V}^{(1)} \cdot \mathbf{n} = 0$. Moreover, when all networks happen to be identical but $N > 1$ (i.e. for some reasons the number of network groups is not reduced to one), then the wave propagation and the associated oscillatory flow are the same in each network, i.e. $p^{(1)} = \cdots = p^{(N)}$ and $\mathbf{V}^{(1)} = \cdots = \mathbf{V}^{(N)}$, cf. the case of a slotted material with identical slits shown in Fig. 1(b). Since all velocity fluxes are identical, in particular at the boundary, the last of the conditions (12) leads to the SHB conditions (11).

We have found that the situation described by conditions (12), or even worse, an imperfect sealing that is only partially similar to it, can occur when the material is not tightly attached to the backing wall (e.g. to the rigid termination of the impedance tube during experiments). This can especially happen when the surface of the material (and/or wall) is rough. To avoid this, the back side of the material must be sealed, e.g. with a thin, impermeable adhesive tape, or glued to the wall.

Conditions analogous to (12) (or, alternatively, to (11)) apply in the general case when a non-zero normal velocity $\hat{v}$ is applied at a boundary of a multiple-network material. When the velocity $\hat{v}$ is specified for the total volumetric flux, this also implies the equalisation of pore network pressures at that boundary, namely

$$p^{(1)} = \cdots = p^{(N)}\,, \qquad \sum_n \mathbf{V}^{(n)} \cdot \mathbf{n} = \hat{v}\,. \tag{13}$$

Recall that these are N conditions, i.e. $(N-1)$ equalities for the pressure fields and one condition that specifies the total flux. An important feature of conditions (12) and (13) is that although the sound pressure of all networks is equalised, no pressure is specified.

Finally, let us consider a situation when all networks of at least one group are closed, i.e. perfectly sealed with rigid plugs on one side of the multiple-network material, see Fig. 4. At the same time, all other networks remain open so that their pressures and velocity fluxes are coupled to the pressure p and particle velocity $\mathbf{v}$ in the adjacent air layer. Let m denotes the types of one-side-closed

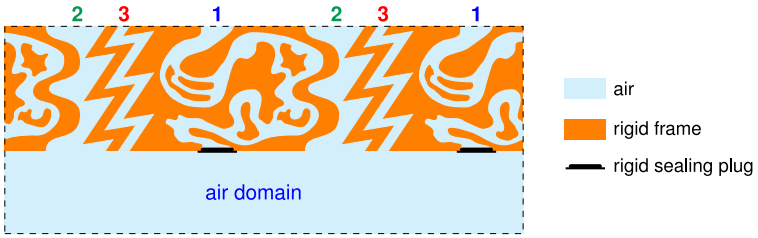

Fig. 4. The edge of the multi-network material with networks of one group (here, networks 1) closed by rigid plugs and other networks open and coupled by the adjacent air domain.

networks ($m = 1$ in the example shown in Fig. 4). The corresponding interface-coupling conditions are expressed by the following $(N + 1)$ equations

$$\forall n \neq m \quad p^{(n)} = p\,, \qquad \sum_{n\neq m} \mathbf{V}^{(n)} \cdot \mathbf{n} = \mathbf{v} \cdot \mathbf{n}\,, \qquad \forall m \quad \mathbf{V}^{(m)} \cdot \mathbf{n} = 0\,. \tag{14}$$

Here, only the pressures of networks open at this interface are equal to p and the sum $\sum_{n\neq m}$ is only over these networks. The sealed networks have zero outward velocity fluxes and – consequently – independent pressures.

2.2.3. *Surface acoustic impedance for a back-sealed or air-gap supported layer*

Analytical solutions are available for plane wave propagation in materials with multiple pore networks, as it is in the case of single-network porous materials. In particular, an analytical formula for the surface acoustic impedance of a porous layer with N separated pore networks sealed at the back of the material, in accordance with the boundary conditions (11), can be derived as follows

$$\mathcal{Z}_{\mathrm{S}} = \frac{p}{\pm \mathbf{v}\cdot\mathbf{n}} = \frac{p}{\pm \sum\limits_n \mathbf{V}^{(n)}\cdot\mathbf{n}} = \frac{1}{\pm \sum\limits_n \frac{\mathbf{V}^{(n)}\cdot\mathbf{n}}{p^{(n)}}} = \frac{1}{\sum\limits_n \frac{1}{\mathcal{Z}_{\mathrm{S}}^{(n)}}}\,. \tag{15}$$

Here, $\mathcal{Z}_{\mathrm{S}}^{(n)}$ is the surface impedance of a porous layer with a *single*-network n, as determined by Eq. (8). It means that for a multiple-network material, $\mathcal{Z}_{\mathrm{S}}$ is calculated as for a hard-backed composite layer with N component materials set in *parallel*, each with a different, single pore network n. Note that the interface conditions (9) on the front face of the multiple-network layer are used to derive formula (15).

The situation becomes more complicated when a layer with separate pore networks is part of a multilayer system, e.g. when it is backed by an air gap. In this case, the pressures from all the disconnected networks are equalised on both sides of the layer. The same thing happens when the multiple-network layer is placed between fluid layers, in particular, effective fluids equivalent to more conventional single-network porous materials. The transfer matrix for a layer with multiple, separated pore networks that takes this into account can be derived as for the parallel assembly of porous components, each having a different pore network n. Verdière et al. [19,44] showed that it is more convenient to work with admittances when the porous elements are in parallel. The transfer matrix for a parallel assembly of N disconnected pore networks has the following form

$$\mathbf{T}^{(\mathcal{P})} = \frac{1}{\sum\limits_n Y_{21}^{(n)}} \begin{bmatrix} -\sum\limits_n Y_{22}^{(n)} & 1 \\ \left(\sum\limits_n Y_{12}^{(n)} \sum\limits_n Y_{21}^{(n)} - \sum\limits_n Y_{11}^{(n)} \sum\limits_n Y_{22}^{(n)}\right) & \sum\limits_n Y_{11}^{(n)} \end{bmatrix}, \tag{16}$$

where $\mathbf{Y}^{(n)}$ is the admittance matrix for a porous layer with network n. It is related to the corresponding transfer matrix $\mathbf{T}^{(n)}$ as follows

$$\mathbf{Y}^{(n)} = \begin{bmatrix} Y_{11}^{(n)} & Y_{12}^{(n)} \\ Y_{21}^{(n)} & Y_{22}^{(n)} \end{bmatrix} = \frac{1}{T_{12}^{(n)}} \begin{bmatrix} T_{22}^{(n)} & \left(T_{12}^{(n)} T_{21}^{(n)} - T_{11}^{(n)} T_{22}^{(n)}\right) \\ 1 & -T_{11}^{(n)} \end{bmatrix} = \frac{1}{T_{12}^{(n)}} \begin{bmatrix} T_{22}^{(n)} & -1 \\ 1 & -T_{11}^{(n)} \end{bmatrix}. \tag{17}$$

The transfer matrix $\mathbf{T}^{(\mathcal{P})}$ is for use in TMM analysis. In particular, $\mathbf{T}^{(\mathcal{P})}$ replaces $\mathbf{T}$ in Eq. (6) for the surface acoustic impedance of a multilayer system with multiple-network material at the front. However, it is very important to notice that for $\mathcal{Z}_{\mathrm{S}}(x_0+\ell) \to \infty$, i.e. when a multiple-network layer is backed by a rigid wall, Eq. (6) with $\mathbf{T} = \mathbf{T}^{(\mathcal{P})}$ does not provide the same result as the formula (15) derived above. This is because instead of boundary conditions (11) which mean that the rigid wall perfectly seals all the networks keeping them separated also at the boundary, the pressure equalisation is realised by the conditions (12) of an infinitely thin layer of air between the material boundary and the wall. Finally, let us recall the case shown in Fig. 4 where some networks are closed and others remain open on one side of the multi-network material adjacent to an air layer. The transfer matrix for this case can also be derived – in the way applied by Verdière et al. [19].

3. Designing multi-tortuous materials: discussion based on examples

3.1. Design procedure and its theoretical foundations

In this and subsequent subsections, we discuss in detail a procedure for designing multi-tortuous materials with multi-resonant behaviour that results in broadband sound absorption in the desired range of relatively low frequencies. This is mainly achieved by adjusting the tortuosity, knowing that by increasing it, the frequency of the associated quarter-wave resonance is lowered [45]. The procedure consists of two stages:

1. Adding separate pore networks into the representative material space of the assumed thickness and tailoring them to obtain contrasting tortuosities that evenly distribute their quarter-wavelength resonances over the desired frequency range.
2. Independent isotropic scaling of the separate networks for impedance matching to achieve additional sound absorption improvement.

An additional goal of tailoring and scaling the pore networks is to fit them tightly inside the representative space of the material to make the total porosity as high as possible, while maintaining the network separation. The proposed technique uses mainly analytical calculations (or semi-analytical at some limited initial stages), which makes it very efficient. This is because the entire design procedure is based on a couple of quite accurate estimation formulas resulting from the theoretical considerations presented below.

The equivalent-fluid approach, and in particular the MPEF model, will be used to analyse wave propagation (see Section 2). This requires determining the effective properties for a material with a pore network n. The dynamic permeabilities, $\mathcal{K}_n$ and Θ_n, necessary for calculating the effective properties (2), are typically determined using frequency-dependent scaling functions that depend on the geometric and transport properties of the porous material, collectively referred to as macro-parameters. Perhaps the most commonly used are the scaling functions of the Johnson–Champoux–Allard–Lafarge–Pride (JCALP) model [1,41,46–48] or its reduced versions, see Appendices B and C. The full JCALP model requires 8 macro-parameters [1]: the open porosity ϕ_n, the kinematic tortuosity $\alpha_{\infty n}$, two static permeabilities (viscous $\mathcal{K}_{0n}$ and thermal Θ_{0n}), two characteristic lengths (viscous $\Lambda_{\mathrm{v}n}$ and thermal $\Lambda_{\mathrm{t}n}$), and two static tortuosities (viscous $\alpha_{0\mathrm{v}n}$ and thermal $\alpha_{0\mathrm{t}n}$).

All tortuosities and characteristic lengths are porosity independent. This is also true for the ratios $\mathcal{K}_{0n}/\phi_n$ and Θ_{0n}/ϕ_n, because both static permeabilities depend on the material porosity in linear way. The same applies to the dynamic permeabilities $\mathcal{K}_n(\omega)$ and $\Theta_n(\omega)$: when divided by ϕ_n they are no longer porosity dependent. Correctly constructed scaling functions ensure this property. Therefore, the effective speed of sound in a porous material

$$c_n(\omega) = \frac{1}{\sqrt{\varrho_n(\omega)\, C_n(\omega)}} = \sqrt{\frac{\mathrm{i}\omega\, \mathcal{K}_n(\omega)}{\eta_{\mathrm{a}}\, C_n(\omega)}} = \sqrt{\frac{\left[\dfrac{\mathcal{K}_n(\omega)}{\phi_n}\right] \dfrac{\mathrm{i}\omega P_0}{\eta_{\mathrm{a}}}}{1 - \left[\dfrac{\Theta_n(\omega)}{\phi_n}\right] \dfrac{(\gamma_{\mathrm{a}}-1)}{\gamma_{\mathrm{a}}} \dfrac{\mathrm{i}\omega}{\tau_{\mathrm{a}}}}} \tag{18}$$

does *not* depend on the material porosity, though it depends on both dynamic permeabilities, but each of them is divided by ϕ_n (see two terms marked with square brackets in the formula above). This fact is not trivial[2] and very important, because to some extent we can design pore networks without prior knowledge (or any assumption) of their porosity, i.e. their volume fraction within the material. This allows to make separate network designs and fit them into the same material space to create a multi-tortuous metamaterial with separated pore networks as demonstrated below.

Let λ_n denotes the wavelength in the porous material with network n. It is determined at frequency f using a standard formula, viz. $\lambda_n(f) = c_{\mathrm{w}n}(f)/f$, in which the wave velocity $c_{\mathrm{w}n} = \mathrm{Re}\, c_n$ is defined as the real part of the effective speed of sound, therefore $\lambda_n(f) = \mathrm{Re}\, c_n(2\pi f)/f$. Now, let $f_{r/4}^{(n,H)}$ denotes the frequency of the r-quarter wavelength resonance (for $r = 1, 3, 5, \ldots$) or antiresonance (for $r = 2, 4, 6, \ldots$) in a layer of thickness H of porous material with network n (or related to this network in the case of materials with several different separated networks). Such resonances (antiresonances) occur for $H = \frac{r}{4}\lambda_n(f)$, i.e. when the layer thickness is an odd (even) multiple of one quarter of the wavelength in the porous material. Sound absorption of the hard-backed porous layer has peaks near the resonant frequencies and troughs near the antiresonant frequencies. This is due to the interference of waves propagating into the porous layer and reflected by the rigid backing.

Finding the resonance or antiresonance frequencies $f_{r/4}^{(n,H)}$ requires solving the following non-linear equation

$$\frac{\mathrm{Re}\, c_n\left(2\pi f_{r/4}^{(n,H)}\right)}{f_{r/4}^{(n,H)}} = \frac{4H}{r} \tag{19}$$

with $r = 1, 3, 5 \ldots$ – for resonances, or $r = 2, 4, 6 \ldots$ – for antiresonances; note that the expression in parentheses is an argument to the function $c_n(\omega)$ defined by Eq. (18). Below we show how those frequencies can be estimated using their upper bounds that depend only on the network tortuosity and speed of sound in air.

[2] Note that ϕ_n is defined as the volume fraction of pores in the volume of the material, and the change in porosity *alone* is due to the change in this fraction only, while neither the shape nor the size of the pore network is modified. Such a change is possible when the pore network is a periodic assembly of subnetworks that are not necessarily identical but are disconnected from each other, so that they can be moved apart or closer together (without overlapping). Changing the pore size or creating new pores and connections would of course affect the speed of sound in the material as well as its permeability and porosity.

The velocity of acoustic waves carried by the air saturating the open pore network is lower than in open air, viz. $c_{\mathrm{w}n}(f) < c_{\mathrm{a}}$. This is due to visco-inertial (and thermal) interactions with the solid skeleton, which slow down wave transmission. In the high frequency range, visco-thermal (but not inertial) effects can be neglected, and the presence of the solid skeleton influences the wave velocity by creating a tortuous path for the oscillating, (almost) inviscid flow through an open pore network. Therefore, the tortuosity of the pore network can be defined at the infinite frequency limit as

$$\alpha_{\infty n} = \lim_{f\to\infty}\left(\frac{c_{\mathrm{a}}}{c_{\mathrm{w}n}(f)}\right)^2 \geqslant 1\,. \tag{20}$$

Incidentally, ultrasonic methods for tortuosity measurement are based on this formula. The airborne wave velocity in an air-saturated porous medium of tortuosity $\alpha_{\infty n}$ is for that reason bounded from above by the following relation:

$$c_{\mathrm{w}n}(f) = \mathrm{Re}\, c_n(2\pi f) < \frac{c_{\mathrm{a}}}{\sqrt{\alpha_{\infty n}}} \tag{21}$$

and $c_{\mathrm{w}n}(f)$ approaches this asymptote monotonically with increasing frequency. As a consequence, the associated wavelength $\lambda_n(f) < c_{\mathrm{a}}/\left(f\sqrt{\alpha_{\infty n}}\right) = \lambda_{\mathrm{a}}(f)/\sqrt{\alpha_{\infty n}}$ is always shorter than $\lambda_{\mathrm{a}}(f) = c_{\mathrm{a}}/f$, i.e. the wavelength in air (in open space). Note that at low frequencies $\lambda_n(f) \ll \lambda_{\mathrm{a}}(f)$ even in the case of not very tortuous conventional acoustic materials, due to significant visco-thermal effects. Basing of these estimations, we can define the upper bound $\widehat{f}^{(n,H)}_{r/4}$ for the r-quarter wavelength resonance and antiresonance frequencies, namely

$$\widehat{f}^{(n,H)}_{r/4} = \frac{r\,c_{\mathrm{a}}}{4H\sqrt{\alpha_{\infty n}}} \;>\; f^{(n,H)}_{r/4} = \frac{r c_{\mathrm{w}n}}{4H}\,. \tag{22}$$

This bound is very useful, because it can be used to estimate the value of $f^{(n,H)}_{r/4}$, with accuracy increasing with the increase in frequency. It is easy to see that for a fixed $\alpha_{\infty n}$, the r-quarter wavelength resonances and antiresonances move to higher frequencies for thinner layers and larger numbers r. However, we found that the proposed estimation can be successfully applied even for $r = 1$ (which is most important when designing) and layers of at least medium thickness. In fact, the following relations apply

$$f^{(n,H)}_{r/4} = \left(1 - \mathcal{E}^{(n,H)}_{r/4}\right)\widehat{f}^{(n,H)}_{r/4} \;\lesssim\; \widehat{f}^{(n,H)}_{r/4} \;<\; f^{(n,H)}_{(r+1)/4} = \left(1 - \mathcal{E}^{(n,H)}_{(r+1)/4}\right)\widehat{f}^{(n,H)}_{(r+1)/4}\,, \tag{23}$$

where the relative errors defined as

$$\mathcal{E}^{(n,H)}_{r/4} \equiv 1 - \frac{f^{(n,H)}_{r/4}}{\widehat{f}^{(n,H)}_{r/4}} \;>\; \mathcal{E}^{(n,H)}_{(r+1)/4} \;>\; 0 \tag{24}$$

are small in most practical cases, while larger errors can be estimated systematically (see Section 3.3).

3.2. Tortuosity-based multi-resonant design

For the purposes of this study, we first designed two networks with highly contrasted tortuosities. These are networks 1 and 2 in Fig. 5(a) which shows their representative periodic fragments. The periodicity is in the direction of wave propagation, which is the vertical direction in Fig. 5. For simplicity, we also assume that – at least at the first stage of design – the period H_{c} is the same for both networks. We set $H_{\mathrm{c}} = 8$ mm and solved the dedicated Laplace, Poisson, and Stokes flow problems [39,40,49,50] for each periodic network to determine macro-parameters required by the JCALP scaling functions. They are listed in Table 1: in columns $\widehat{1}$ and 1 – for network 1, and columns $\widehat{2}$ and 2 – for network 2. Recall that the static permeabilities can be calculated when the porosity ϕ_n is known. To this end, the size of the periodic unit cell, a.k.a. representative elementary volume (REV), containing the pore network needs to be specified first. Fig. 5(b) shows two rectangular unit cells: REV $\widehat{1}$ and REV $\widehat{2}$ – one for each of the two networks. These REVs have the same size $H_{\mathrm{c}} \times \widehat{W}_{\mathrm{c}}$, where the cell width is $\widehat{W}_{\mathrm{c}} = 1.65H_{\mathrm{c}} = 13.2$ mm. This width is large enough to accommodate both networks, still keeping them separated, so that a new combined REV $\widehat{1}$+$\widehat{2}$ for the dual-tortuosity material can be created, see the third unit cell in Fig. 5(b). It represents the actual geometry of the multi-tortuous material, but the appropriate multi-pressure modelling requires separate calculations on REV $\widehat{1}$ and REV $\widehat{2}$ only. The porosities and static permeabilities calculated for these two REVs are given in Table 1, in columns $\widehat{1}$ and $\widehat{2}$, respectively. Two complete sets of macro-parameters were used to determine the dynamic viscous and thermal permeabilities using the JCALP scaling functions [39,40], see Appendix B. Then, the effective properties of two fluids acoustically equivalent to single-network materials $\widehat{1}$ and $\widehat{2}$ were calculated.

Fig. 6(a) shows sound absorption at normal incidence calculated for porous layers backed by a rigid wall, see Appendix A. The results for three porous materials described above are compared, namely two materials with single tortuosity and the dual-tortuosity material. In each case, the layer thickness $H = 5H_{\mathrm{c}} = 40$ mm is the same, so the direct comparison makes sense. The blue dotted curve shows absorption for the single-tortuosity material based on REV $\widehat{1}$. In the frequency range of interest, i.e. below 2.4 kHz, this curve exhibits two peaks at the designed frequencies of one-quarter and three-quarter wavelength resonances. The absorption at the first, i.e. low-frequency peak exceeds 0.9. Sound absorption for material $\widehat{2}$ is shown by a green dash-dotted curve with the maximum value greater than 0.8 at a predicted frequency corresponding to the quarter wavelength resonance determined for the layer with pore network 2. Finally, the continuous orange curve presents sound absorption at normal incidence by the dual-tortuosity layer based on REV $\widehat{1}$+$\widehat{2}$. This absorption curve combines the performance obtained by the two single-tortuosity materials. In particular, it has three peaks at the designed frequencies. This result is validated by the numerical solution of the Navier–Stokes equations (see Section 4.2 for more information about such direct numerical simulations). It is worth noting the good absorption between

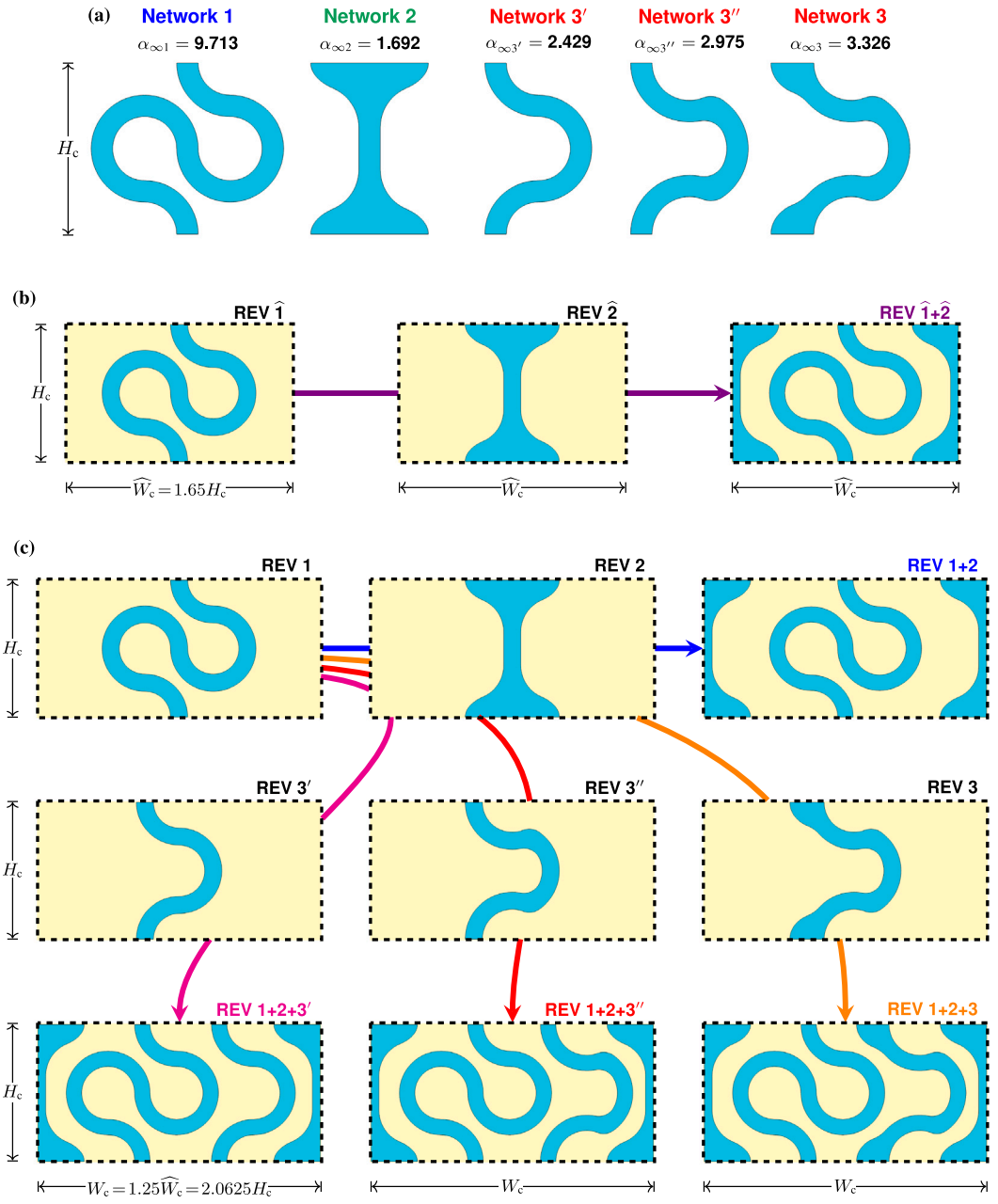

Fig. 5. Two-dimensional pore networks and the construction of representative elementary volumes (REVs) containing them.

the second and third peaks, spanning an almost 300 Hz range, with the lowest absorption value only slightly below 0.6. On the other hand, there is a wide frequency range with rather poor absorption between the first and second absorption peaks. In order to improve it, a third pore network can be designed and added to create a multi-resonant material with triple tortuosity.

The third pore network was designed in three variants denoted by 3′, 3″ and 3, see Fig. 5(a) and also the corresponding REVs in the middle row of Fig. 5(c). We started with network 3′ which has the form of a gently winding channel of constant width. Therefore, we could analytically estimate its tortuosity $\alpha_{\infty 3'}$ as the square ratio of the channel length to its unit cell height H_c [10,51]. This analytical assessment of tortuosity is very accurate for constant-width channels (it also worked for network 1) and as intended: $\alpha_{\infty 1} > \alpha_{\infty 3'} > \alpha_{\infty 2}$. Using formula (22) (with $r = 1$ and $n = 3'$) we estimated the quarter-wavelength resonance frequency for a 40 mm layer with network 3′. We found it to be too high, so we slightly modified the channel by making it more tortuous (network 3″) and then we also increased its width in some places (network 3). The goal was to increase the tortuoisty so that the

Table 1
Macro-parameters calculated for pore networks and REVs (see Fig. 5).

Parameter	(Unit)	$\widehat{1}$	1	$\widehat{2}$	2	3′	3″	3
$\alpha_{\infty n}$	(–)	9.713		1.692		2.429	2.975	3.326
$\alpha_{0\mathrm{v}n}$	(–)	11.73		2.054		2.933	3.597	4.031
$\alpha_{0\mathrm{t}n}$	(–)	1.201		1.520		1.201	1.208	1.507
$\Lambda_{\mathrm{v}n}$	(mm)	0.873		1.097		0.873	0.883	0.922
$\Lambda_{\mathrm{t}n}$	(mm)	0.900		1.859		0.900	0.917	1.035
$\mathcal{K}_{0n}/\phi_n$	(10^{-9} m^2)	6.803		55.60		27.20	22.80	22.06
Θ_{0n}/ϕ_n	(10^{-9} m^2)	67.73		468.3		67.72	70.71	104.6
ϕ_n	(%)	21.42	17.14	17.55	14.04	8.568	9.684	11.43
$\mathcal{K}_{0n}$	(10^{-9} m^2)	1.457	1.166	9.756	7.805	2.331	2.208	2.520
Θ_{0n}	(10^{-9} m^2)	14.51	11.61	82.18	65.74	5.803	6.848	11.95

quarter-wavelength resonance frequency associated with this new network is midway between the resonance frequencies associated with networks 1 and 2. We achieved that with network 3 (this time $\alpha_{\infty 3} = 3.326$ was determined by solving the dedicated Laplace problem [39,40,49]). This three-variant approach is illustrated by the corresponding results shown in Fig. 6(b) and discussed below.

The shape of the third network was chosen to fit neatly between networks 1 and 2, as depicted in the bottom row of Fig. 5(c). However, to make it possible and also 3D printable (see Section 4.1), the cell width had to be enlarged by 25%. The new width is therefore $W_\mathrm{c} = 1.25\widehat{W}_\mathrm{c} = 16.5$ mm. The macro-parameters for all three variants of the third network are listed in the last three columns of Table 1. Table 1 also gives new values of porosity and static permeabilities for REV 1 and REV 2 shown in the first row of Fig. 5(c). Fig. 6(b) shows sound absorption calculated for 40 mm layers with single pore networks. First, it should be noted that the absorption curves obtained for the two materials based on REV 1 and REV 2 are very similar to their counterparts based on REV $\widehat{1}$ and REV $\widehat{2}$, respectively. In particular the resonance frequencies are – as expected – exactly the same, cf. blue and green curves, respectively, between graphs (a) and (b) in Fig. 6. However, in the case of network 1 the peak values slightly dropped, cf. blue curves between graphs (a) and (b) in Fig. 6, while the peak value increased to almost 0.9 in the case of material with network 2, cf. green curves between graphs (a) and (b) in Fig. 6. As for the third network material, the results for the three variants shown in the middle row of Fig. 5(c) are compared to show that the absorption peak shifts towards lower frequency with increasing tortuosity.

Fig. 6(c) shows sound absorption at normal wave incidence (see Appendix A) calculated for two triple-tortuosity materials based on REV 1+2+3′ and REV 1+2+3, see also the bottom row of Fig. 5(c). For clarity of the graph we have omitted the curve for REV 1+2+3″. As intended, we now have four resonant absorption peaks in the considered frequency range and the precisely selected frequency of the absorption peak related to the third network is achieved with excellent accuracy. The semi-analytical results are verified by direct Navier–Stokes simulations (see Section 4.2). In addition, to confirm the multi-resonance origin of the absorption peaks, we show the absorption curves calculated for the three single-tortuosity materials based on REV 1, REV 2, and REV 3, respectively. This time, they were also determined using Navier–Stokes simulations, but they are very similar to their counterparts calculated by the semi-analytical method, cf. the corresponding absorption curves between graphs (b) and (c) in Fig. 6. Finally, it should be noted that the previously observed weak absorption between the peaks has generally improved. It is therefore evident that very good broadband absorption in the desired frequency range can be achieved in this way, i.e. by adding yet another precisely tailored network.

3.3. Isotropic scaling for impedance matching

Fig. 7(a) compares the relative size of REV 1+2+3 with its isotropically scaled variants. For the sake of further comparisons, we consider the following scaling factors: $s = 0.5$, 0.625, 1.0 (i.e. no scaling), and 1.25. For these scales, the following integers, i.e. number of cells $N_\mathrm{c} = 10$, 8, 5, and 4, respectively, ensure the same layer thickness $H = N_\mathrm{c} s H_\mathrm{c} = 40$ mm.

Isotropic scaling does not change the shape of REV, so the porosity and tortuosity of the material remain unchanged. Only the characteristic lengths and static permeabilities are modified. Table 2 lists the new values of these parameters recalculated numerically for the isotropically scaled versions of REV 1, REV 2, and REV 3. Note the quadratic change of the permeabilities with respect to the scaling factor s, while the characteristic lengths change linearly. The following modifications apply with respect to the values listed in Table 1 and determined for unscaled REV (i.e. for $s = 1$):

$$\Lambda_{\mathrm{v}n}(s) := s\Lambda_{\mathrm{v}n}(1), \quad \Lambda_{\mathrm{t}n}(s) := s\Lambda_{\mathrm{t}n}(1), \qquad \mathcal{K}_{0n}(s) := s^2\mathcal{K}_{0n}(1), \quad \Theta_{0n}(s) := s^2\Theta_{0n}(1). \tag{25}$$

Isotropic scaling affects the wave velocity. For $s < 1$ the pores and channels become smaller and narrower, increasing the viscous effects that slow down the wave. The opposite occurs for $s > 1$. Assuming that the layer thickness H is intact, the r-quarter wavelength resonances and antiresonances are shifted to lower frequencies for $s < 1$, or to (slightly) higher frequencies for $s > 1$. Table 3 compares the frequencies of one-quarter and three-quarter wavelength resonances determined for 40 mm thick layers based on single-tortuosity REVs with different isotropic scaling. The s-independent upper-bound-based estimates are also given along with the corresponding errors. As explained above, the resonance and antiresonances frequencies change with s. We propose the following formula to predict these changes:

$$f_{r/4}^{(n,H)} \approx \left(1 - \frac{\mathcal{E}_{r/4}^{(n,H)}}{s}\right)\widehat{f}_{r/4}^{(n,H)} = \left(1 - \widetilde{\mathcal{E}}_{r/4}^{(n,H)}\right)\widehat{f}_{r/4}^{(n,H)}. \tag{26}$$

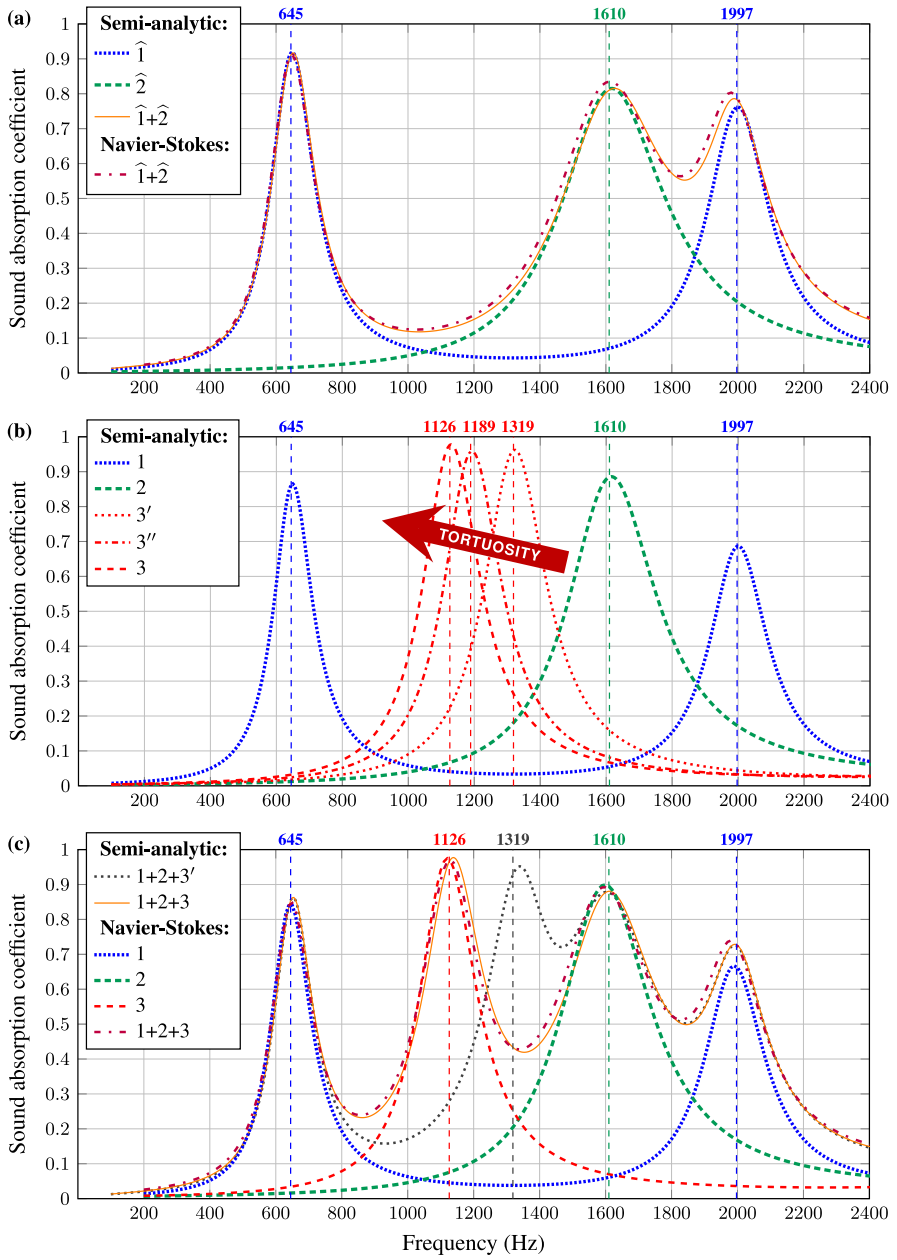

Fig. 6. Sound absorption predictions for 40 mm-thick porous layers illustrating the design process of multi-tortuous metamaterials based on the networks and REVs depicted in Fig. 5.

Table 2
The characteristic lengths and static permeabilities for isotropically scaled REV 1, REV 2, and REV 3.

Parameter	(Unit)	s=**0.5** (sH_c=4 mm)			s=**0.625** (sH_c=5 mm)			s=**1.25** (sH_c=10 mm)		
		1	2	3	1	2	3	1	2	3
Λ_{vn}	(mm)	0.437	0.549	0.461	0.546	0.686	0.576	1.092	1.372	1.152
Λ_{tn}	(mm)	0.450	0.930	0.518	0.563	1.162	0.647	1.125	2.324	1.294
$\mathcal{K}_{0n}$	(10^{-9} m^2)	0.291	1.951	0.630	0.455	3.049	0.985	1.821	12.20	3.938
Θ_{0n}	(10^{-9} m^2)	2.901	16.44	2.989	4.533	25.68	4.670	18.13	102.7	18.68

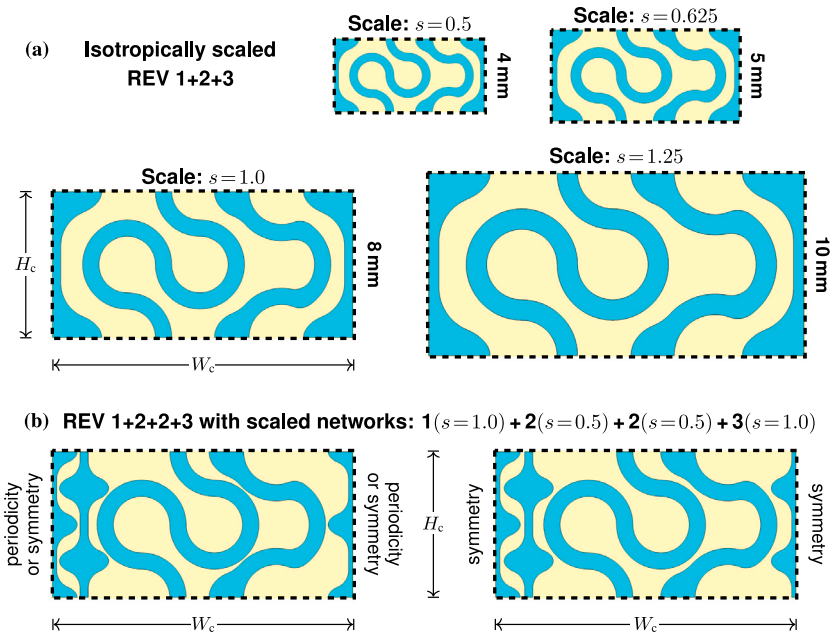

Fig. 7. Representative unit cells with isotropically scaled networks.

Table 3
Frequencies of the one- and three-quarter wavelength resonances (along with the corresponding upper-bound-based estimates and their relative errors, as well as relative error predictions) for hard-backed porous layers composed of the specified REV (see Fig. 5) scaled by s, for the layer thickness $H = N_c s H_c = 40$ mm.

REV n:	1				2				3′	3″	3			
Scale s:	0.5	0.625	1.0	1.25	0.5	0.625	1.0	1.25	1.0	1.0	0.5	0.625	1.0	1.25
sH_c (mm):	4	5	8	10	4	5	8	10	8	8	4	5	8	10
N_c:	10	8	5	4	10	8	5	4	5	5	10	8	5	4
$f_{1/4}^{(n,H)}$ (Hz):	594	616	645	655	1556	1578	1610	1621	1319	1189	1064	1089	1126	1138
$\widehat{f}_{1/4}^{(n,H)}$ (Hz):	694				1663				1388	1254	1186			
$\mathcal{E}_{1/4}^{(n,H)}$ (%):	14.41	11.24	7.06	5.62	6.43	5.11	3.19	2.53	4.97	5.18	10.29	8.18	5.06	4.05
$\widetilde{\mathcal{E}}_{1/4}^{(n,H)}$ (%):	14.12	11.30	7.06	5.65	6.37	5.10	3.19	2.55	4.97	5.18	10.12	8.09	5.06	4.05
$f_{3/4}^{(n,H)}$ (Hz):	1914	1947	1997	2014	4805	4842	4898	4916	4044	3650	3350	3392	3455	3476
$\widehat{f}_{3/4}^{(n,H)}$ (Hz):	2082				4989				4164	3763	3559			
$\mathcal{E}_{3/4}^{(n,H)}$ (%):	8.07	6.48	4.08	3.27	3.69	2.95	1.82	1.46	2.88	3.00	5.87	4.69	2.92	2.33
$\widetilde{\mathcal{E}}_{3/4}^{(n,H)}$ (%):	8.17	6.53	4.08	3.27	3.65	2.92	1.82	1.46	2.88	3.00	5.84	4.68	2.92	2.34

Here, $\widetilde{\mathcal{E}}_{r/4}^{(n,H)} = \frac{1}{s}\mathcal{E}_{r/4}^{(n,H)}$ is the relative error prediction that takes into account isotropic scaling. This correction is very accurate, cf. $\widetilde{\mathcal{E}}_{r/4}^{(n,H)}$ with $\mathcal{E}_{r/4}^{(n,H)}$ ($r = 1, 3$) in Table 3. The formula (26) is extremely useful for controlling changes in target frequencies due to isotropic scaling. For example, the exact value of $f_{1/4}^{(1,H)} = 645$ Hz was calculated for REV 1 in its original size ($s = 1$) by solving equation (19). It is by $\mathcal{E}_{1/4}^{(1,H)} = 7.06\%$ lower than its estimate $\widehat{f}_{1/4}^{(1,H)} = 694$ Hz, determined using the upper-bound formula (22). After isotropic scaling by $s = 0.5$, we expect the error to be twice as large, i.e. the corrected prediction of this error is $\widetilde{\mathcal{E}}_{1/4}^{(1,H)} = 14.12\%$. We can use it to find an approximated value (26) of the modified frequency, namely $f_{1/4}^{(1,H)} \approx 596$ Hz. All this is done without recalculating the static permeabilities and characteristic lengths and solving the non-linear equation (19). Of course, we can eventually do this to find that the approximate frequency is only a negligible 2 Hz greater than the exact value of $f_{1/4}^{(1,H)} = 594$ Hz.

Fig. 8(a) compares sound absorption (see Appendix A) calculated for isotropically scaled REV 1+2+3, in which each network was isotropically scaled by the same factor $s = 0.5$, 0.625, 1.0 (no scaling), or 1.25, as illustrated in Fig. 7(a). For $s < 1$ the absorption peaks and troughs are shifted towards slightly lower frequencies, whereas for $s > 1$ they are shifted towards slightly

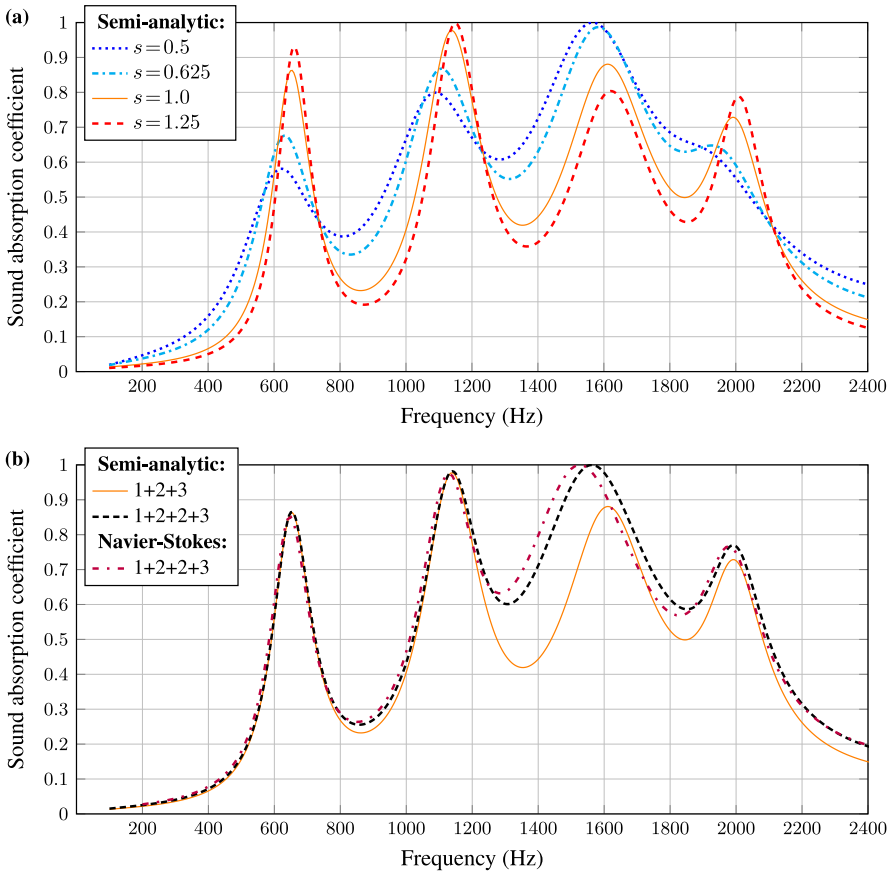

Fig. 8. Sound absorption predictions for 40 mm-thick layers based on multi-tortuous metamaterial designs shown in Fig. 7.

higher frequencies, compared to the case without scaling ($s = 1.0$). In each case, all new frequency values are predictable by the proposed formula (26). The impact on the absorption value is less predictable and requires full calculations. One should observe, however, that when the considered geometry is scaled by $s < 1$, the low absorption values in the troughs increase significantly, while at the same time the peak values decrease, except for the third peak that is related to network 2. It is therefore obvious that an optimal improvement can be achieved by different isotropic scaling of each network separately. Various design criteria can be applied, e.g. perfect absorption in peaks, improved absorption in troughs. Here we propose scaling the selected network to achieve perfect absorption at the first peak related to it by matching the surface impedance at the peak frequency to the characteristic impedance of air, namely

$$\mathcal{Z}_{\mathrm{S}}^{(n)}\left(2\pi f_{1/4}^{(n,H)}\right) \approx Z_{\mathrm{a}} \tag{27}$$

where $\mathcal{Z}_{\mathrm{S}}^{(n)}(\omega) = \varrho_n(\omega)c_n(\omega)\coth\left(\mathrm{i}\omega H/c_n(\omega)\right)$ is computed for the single-tortuosity layer with scaled network n (see Eq. (8)), because for multi-tortuous materials with evenly distributed resonances: $\mathcal{Z}_{\mathrm{S}} \approx \mathcal{Z}_{\mathrm{S}}^{(n)}$ at $f_{1/4}^{(n,H)}$. In other words, we isotropically scale network n by factor s so that for the assumed layer thickness H: $\mathrm{Re}\,\mathcal{Z}_{\mathrm{S}}^{(n)} \approx Z_{\mathrm{a}}$ and $\mathrm{Im}\,\mathcal{Z}_{\mathrm{S}}^{(n)} \approx 0$ at the quarter-wavelength resonance frequency $f_{1/4}^{(n,H)}$. This creates a quasi anechoic condition for plane harmonic waves of this frequency propagating in air onto the porous layer, which means that the surface of the layer does not reflect such waves perpendicularly incident to it. The impedance-matching procedure can be applied for all networks simultaneously. Recall, however, that the scaled networks should also be re-arranged without overlapping within the layer space of thickness H.

The condition (27) is satisfied for network 2 after isotropic scaling by factor $s = 0.5$. We managed to replace the original network 2 by its scaled counterparts inside the original REV with dimensions $W_{\mathrm{c}} \times H_{\mathrm{c}}$, as illustrated by two variants shown in Fig. 7(b). In both cases, the networks are very close to each other to maintain the REV dimensions, but they do not overlap, although in the left-hand-side variant this requirement is barely met. The distances between networks are slightly larger in the right-hand-side variant, but this network arrangement assumes symmetry on the lateral edges of the unit cell. The differences between the network arrangement variants are not grasp by the semi-analytical modelling, so we use the same label REV 1+2+2+3 for both. We have also checked that direct numerical simulations based on the Navier–Stokes equations give practically the same sound absorption curves

for both variants. Note that the total porosity of REV, as well as its dimensions, also remains unchanged. Therefore, the results obtained for the multi-tortuous material constructed from REV 1+2+2+3 can be directly compared with those determined for the original designs based on REV 1+2+3. We do it in Fig. 8(b) to conclude that sound absorption in the entire considered frequency range is better for the material with scaled network 2. However, below 1.2 kHz the two absorption curves are almost identical, cf. two semi-analytic curves in Fig. 8(b). Then, the expected improvement in absorption is achieved over a wide frequency range around the third peak related to the scaled network 2. The curves become almost identical again at frequencies above 2 kHz, after the fourth peak. The semi-analytical results are confirmed by the aforementioned Navier–Stokes simulations. Finally, we have found that the third sound absorption peak reaches an almost perfect value of 0.9996 at a frequency of 1560 Hz (note that $f_{1/4}^{(2,H)} = 1556$ Hz), where the real and imaginary parts of the normalised (i.e. divided by Z_a) surface acoustic impedance of the multi-tortuous layer are: $\mathrm{Re}\, \mathcal{Z}_S/Z_a = 1.036 \approx 1$ and $\mathrm{Im}\, \mathcal{Z}_S/Z_a = -0.019 \approx 0$.

4. Experimental and numerical validation

4.1. 3D printed sample and three case studies

A sample of multi-tortuous material based on REV 1+2+2+3 was 3D printed using stereolithography technology from a transparent photopolymer resin of low viscosity. The material thickness is $H = 5H_c = 40$ mm. Fig. 9 shows several pictures of this sample, namely: three scans made with a flatbed scanner (on the left) and three photographs (on the right). The sample was printed in the form of a 80×80×40 mm cuboid with wide clamping edges for mounting it to a 66 mm square impedance tube, see Fig. 9(a,b,c). The clamp mounting ensures no sound leakage around the sample during experimental tests. There are twelve 66 mm-long slits on

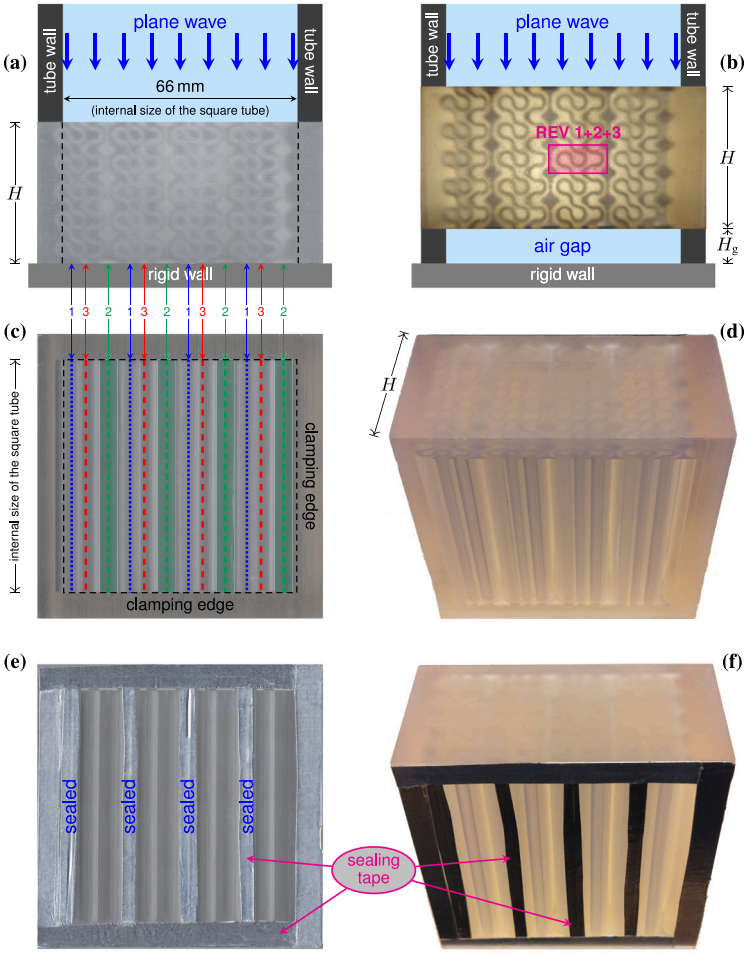

Fig. 9. 3D printed sample of multi-tortuous acoustic metamaterial: (a,b) side views (scan and photo, respectively) showing the sample mounting to the square impedance tube with (a) rigid wall or (b) air gap backing; (c,d) front views (scan and photo); (e,f) rear views (scan and photo) with network 1 sealed with adhesive tape.

the front and back surfaces of the sample. These are the entries to the pore networks arranged periodically in four groups of three, within a square area with an edge dimension of $4W_c = 66$ mm, which is the internal size of the square tube. Thus, all pore networks are open to plane acoustic waves propagating in the impedance tube at normal incidence to the sample surface. For better visibility, the slotted entries to the pore networks are marked with blue (network 1), green (network 2), and red lines (network 3) in Fig. 9(c).

Sound absorption at normal incidence was measured for the 3D printed sample using a 66 mm square impedance tube and two-microphone transfer function method [52]. Three cases were studied:

1. **Case A:** the multi-tortuous material is backed by a rigid wall, see Fig. 9(a);
2. **Case B:** the multi-tortuous material is backed by an air gap, see Fig. 9(b);
3. **Case C:** the multi-tortuous material is backed by an air gap as depicted in Fig. 9(b), but the rear entries to pore networks 1 are sealed with adhesive tape, see Fig. 9(e,f).

Note that the first case study is the perfectly-sealed hard-backed layer configuration that was used to design the triple-tortuosity material in Section 3.2. Cases B and C include a backing air gap of a thickness $H_g = 10$ mm, so that the total thickness of such a two-layer configuration is $H + H_g = 50$ mm.

4.2. Numerical methods used

We applied two numerical approaches to verify semi-analytical analyses of multi-tortuous materials:

1. **MPEF** – the Multi-Pressure Equivalent Fluid numerical model, introduced in Section 2.2, which contains N Helmholtz equations coupled by equal-pressure conditions at air interfaces or on Dirichlet boundaries;
2. **DNS** – Direct Numerical Simulation based on the solution of linearised Navier–Stokes equations.

Both approaches use the Finite Element (FE) method. They are much more versatile than the semi-analytical calculations which can only be used to study the propagation of plane waves at normal incidence, investigated in this work. In particular, the linearised Navier–Stokes DNS can, under certain conditions, be considered as a numerical equivalent of the experiment. However, such fully-coupled Navier–Stokes simulations can be computationally very demanding for three-dimensional and even two-dimensional problems. Thanks to the MPEF model, they are not required and are used only for additional verification purposes.

The proposed MPEF method is based on homogenisation and is therefore numerically very efficient. The scheme of this method is depicted in Fig. 10 for the triple-tortuosity material in the three configurations considered. In each case there are three parallel domains or rather fully overlapping but independent layers of equivalent fluids (thickness $H = 40$ mm), namely: EF 1 representing the material with network 1 (based on REV 1), EF 2 for the material with network 2 (REV 2), and EF 3 for the material with network 3 (REV 3). At their upper boundaries, they are coupled by conditions (9) with the adjacent air domain. This air domain

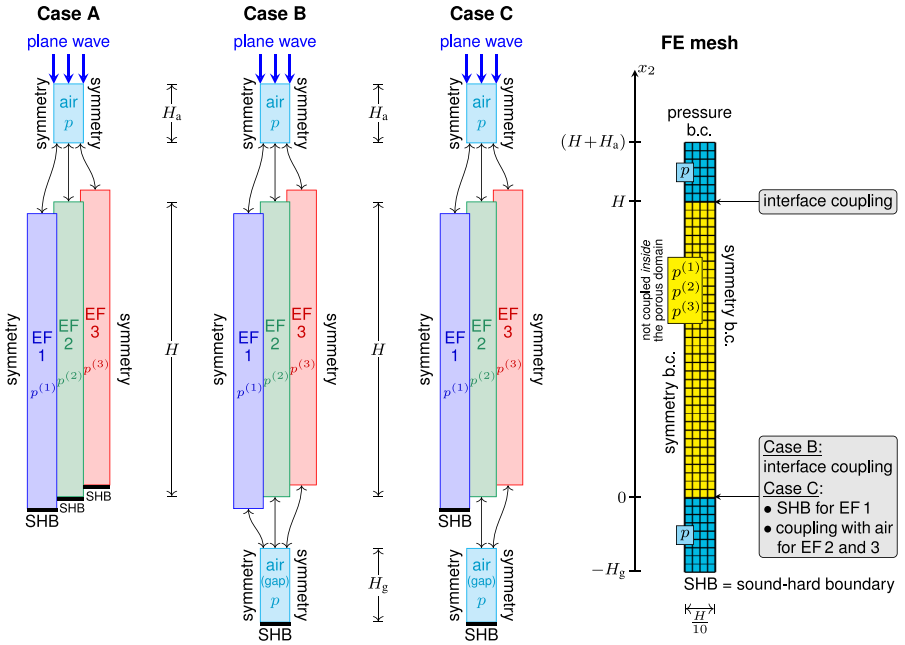

Fig. 10. Case studies for the MPEF model.

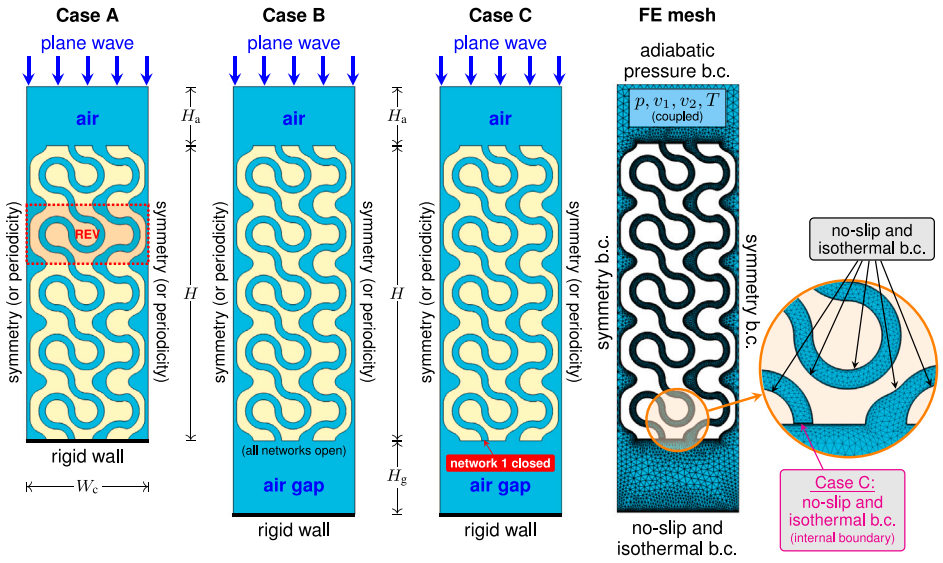

Fig. 11. Case studies for the linearised Navier–Stokes simulations.

thickness (height) is $H_a = 8$ mm. A pressure of $\hat{p} = 1$ Pa is applied at its upper boundary to simulate the incidence of a plane acoustic wave. In Case A, the sound-hard boundary (SHB) condition (11) is applied at the lower boundary of each EF domain to simulate the rigid wall support with perfect sealing bond. In Case B, these boundary conditions are replaced by the interface coupling (9) with the air-gap domain. Case C is special because the SHB condition is applied on the lower boundary of EF 1 to simulate perfect sealing, while EF 2 and EF 3 are coupled with the air gap. The air gap thickness (height) is $H_g = 10$ mm and the SHB condition is applied on its lower, i.e. rigid-wall boundary. Fig. 10 also shows the FE mesh used to analyse Cases B and C. The homogenised problem configuration is essentially one-dimensional, but the mesh used for this numerical validation is two-dimensional and has a width of $\frac{1}{10}H = 4$ mm that was assumed arbitrarily. Symmetry conditions are applied on all lateral boundaries. A similar mesh, but without the air gap domain, was used for Case A. Note that three different Helmholtz problems are solved using the same FE mesh of porous material marked in yellow in Fig. 10. The coupling between these problems only occurs at the interfaces with the air domains, also modelled by the Helmholtz equation.

Fig. 11 shows three schemes used by Navier–Stokes simulations for the three case studies. In each case, two-dimensional geometry of the triple-tortuous material is accurately represented by periodic repetition of its unit cell, i.e. REV 1+2+3, along the layer thickness. One instance of this REV is highlighted in Case A. The three separate networks are saturated with air. They are in fact connected but only *outside* the porous layer of thickness $H = N_c H_c = 40$ mm, namely: through the adjacent air layer (thickness $H_a = 8$ mm) directly above the porous layer, as well as – additionally in Cases B and C – through the air gap (thickness $H_g = 10$ mm) below the layer. In Case C, the air gap only connects networks 2 and 3, while network 1 is closed at this end to simulate sealing with adhesive tape on the back of the porous material, as shown in Fig. 9(e,f) for all four instances of network 1. The computational domain width is $W_c = 16.5$ mm, i.e. equal to the REV width. Symmetry or periodicity conditions are applied on its lateral boundaries; we have checked that practically the same results are obtained in terms of sound absorption. No-slip and isothermal boundary conditions are applied on all solid boundaries (i.e. rigid skeleton and backing wall), while adiabatic pressure condition (with $\hat{p} = 1$ Pa) on the top air boundary. All these conditions are marked on the FE mesh for Case C presented in Fig. 11. This and similar FE meshes were used to solve (at each computational frequency) the harmonic Navier–Stokes equations of visco-thermal flow, for four coupled, complex-valued, degrees of freedom, viz.: acoustic pressure p, two velocity components, v_1 and v_2, and temperature T.

Sound absorption at normal incidence is determined in a similar manner for FE solutions of the MPEF problem and the Navier–Stokes DNS. In both cases, it is necessary to first calculate the surface acoustic impedance and then determine the sound reflection and absorption coefficients in a standard way [1], see Appendix A for details.

The sound absorption results calculated using DNS for Case A have already been presented in Section 3 for the triple-tortuosity layer, and also for single-tortuosity materials as well as for the triple-tortuosity material with one of the networks isotropically scaled. In the following section, we discuss and compare the MPEF and DNS results obtained for all three case studies and confront them with experimental results.

4.3. Discussion of sound absorption results

Sound absorption at normal incidence measured on the 3D printed sample backed by a rigid wall (i.e. for Case A configuration) is presented in Fig. 12 along with the corresponding predictions by semi-analytical calculations and both FE analyses. The

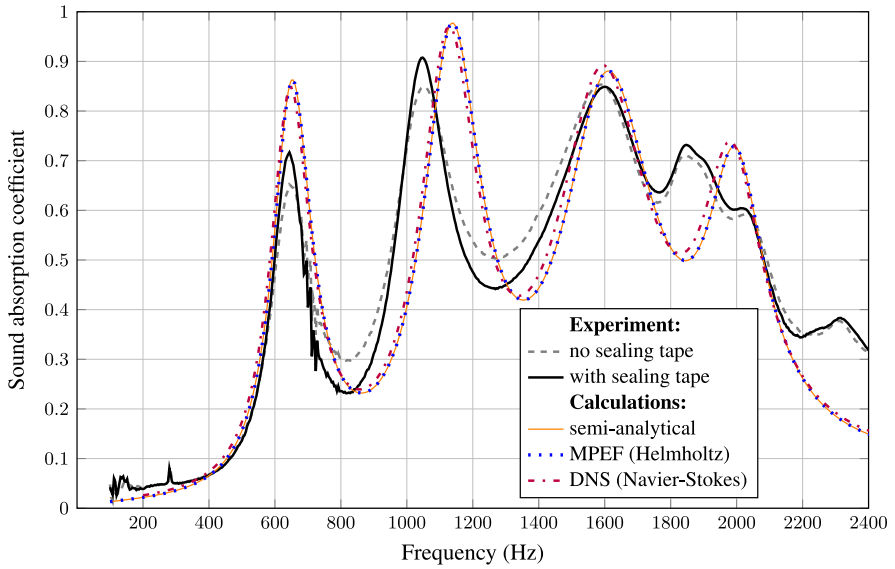

Fig. 12. Sound absorption calculated and measured for the 40 mm-thick sample of multi-tortuous metamaterial.

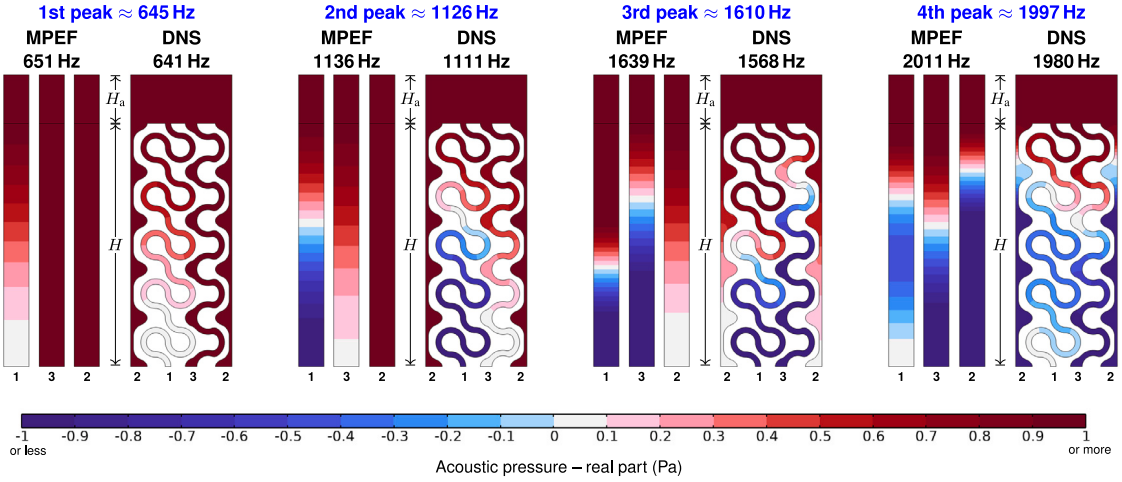

Fig. 13. Acoustic pressure (real part) distributions at sound absorption peaks (Case A).

pressure distributions calculated by these numerical analyses are shown in Fig. 13. The modelling (by all methods) anticipated the experimental results well. In particular, the multi-resonant behaviour, evidenced by the four absorption peaks, is very well predicted. Inaccuracies in predicting the frequency of individual absorption peaks should be confronted with the quality of each 3D printed network, assessing compliance with the shape used to calculate the corresponding macro-parameters. Noticeable discrepancies concern the second absorption peak. This peak is associated with network 3 and occurs at a frequency that is about 80 Hz lower than the predicted value, which means that the actual tortuosity of this network is slightly larger than the calculated value.

All in all, the discrepancies between the measurements and predictions are due to 3D printing imperfections and sound leakages [53]. To illustrate the latter, we present two experimental results labelled as “no sealing tape” and “with sealing tape” in Fig. 12. During the first of these tests, the back of the sample was fixed directly to a thick aluminium plate to realise rigid-wall support. The measurement was then repeated “with sealing tape”, meaning that before fixing the aluminium plate, the entire back side of the sample was carefully sealed with a thin, adhesive aluminium tape. It is evident that the results obtained in the first test are less accurate and even greater discrepancies occurred when the aluminium plate was not fastened tightly enough (for clarity of the graph, we have omitted these more inaccurate results). This was caused by sound leakages between the pore networks at the

back of the sample, possibly leading to some pressure equalisation. Additional securing of the back side of the sample with adhesive tape solved this problem.

In the extreme case, when a very thin layer of air forms at the back of the sample which is too loosely attached to the rigid wall and not secured with a tape, the network pressures can be completely equalised according to the conditions (12). As a result, sound absorption can be dramatically different from the case when the networks are sealed at the back of the sample. The same problem can occur when the multiple-network layer is formed, e.g. from two identical but unbounded samples: the networks can be connected at the interface and their pressures equalised, leading to unexpected results. Recall that imperfect interfaces in multilayer systems of conventional acoustic materials may also have a non-negligible effect on sound absorption [54].

The results obtained using the numerical MPEF model are in a perfect agreement with the semi-analytical calculations: the blue dotted curve practically overlaps the continuous orange curve in Fig. 12. This was expected since both methods are closely related and based on the same equivalent fluids defined by the same sets of macro-parameters given in Table 1. The DNS results are also in almost perfect agreement with these predictions, although in this case the absorption peaks are shifted to slightly lower frequencies than predicted by previous methods. The results by the MPEF model and DNS are also compared in Fig. 13 which presents the distribution of the real part of the acoustic pressure inside the parallel smeared-network subdomains of equivalent fluids (MPEF) and the geometrically accurate pore networks (DNS). The pressure distributions are shown at frequencies close to absorption peaks. It is clearly seen that a pressure node (i.e. zero pressure) is formed at the back of the pore network n and its corresponding equivalent-fluid domain n, with: $n = 1$ for the 1st and 4th absorption peaks, $n = 3$ for the 2nd absorption peak, and $n = 2$ for the 3rd peak. Thus, each absorption peak occurs in the quarter-wavelength resonance of the corresponding pore network. In the case of the 4th absorption peak it is actually a three-quarter-wavelength resonance of network 1 (note the additional pressure node inside the pore network 1 and its equivalent fluid 1, at a distance of about $\frac{1}{3}H$ from the front, i.e. top surface of the layer).

The sound absorption curves determined for Cases B and C are presented in Fig. 14(a) and (b), respectively. As for Case A, the absorption results calculated for the configurations with an air gap using the numerical MPEF model or semi-analytical calculations match perfectly. These curves completely overlap and differ only slightly from the absorption curve obtained by DNS. More importantly, the modelling results, although rather unusual, are fully confirmed by measurements. One should notice the very

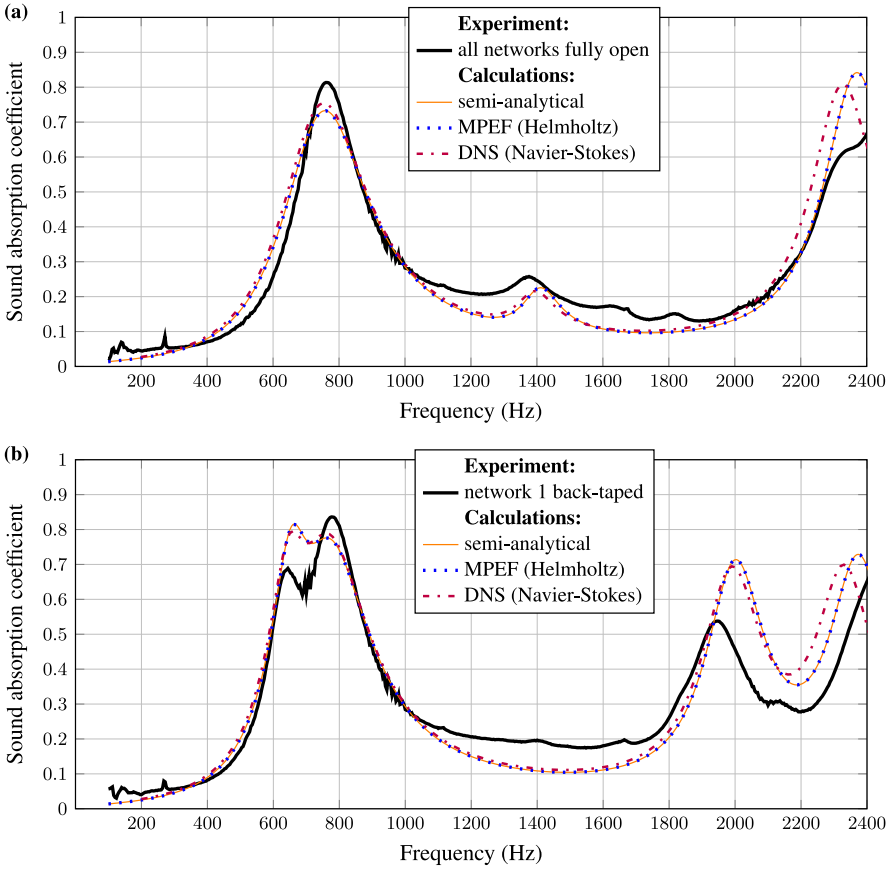

Fig. 14. Sound absorption by the 40 mm-thick sample of multi-tortuous metamaterial backed with a 10 mm air gap, for: (a) all networks fully open, or (b) network 1 taped at the back of the sample.

uncommon change in absorption after adding an air gap. It is well known that adding an air gap behind a porous layer made of conventional, i.e. single-tortuosity acoustic material should cause all absorption peaks to shift to lower frequencies [1]. If the air gap layer is thick enough, new peaks may appear in the considered frequency range, shifted from frequencies above this range. All this does not happen when the triple-tortuosity layer is supported by an air gap! On the contrary, in Case B the first absorption peak occurs at about 760 Hz, which is a good 100 Hz higher than the first peak frequency in the gap-less configuration of Case A, cf. the absorption curves between Figs. 14(a) and 12. Then, a significant peak in absorption appears at a frequency just below the 2.4 kHz range limit. There is also a very small peak in-between, at around 1.4 kHz, which could be mistaken for a measurement artefact if it were not predicted by the modelling, see Fig. 14(a). This atypical behaviour is discussed in more detail in Section 4.4.

In Case C, network 1 is sealed at the back of the sample. As a consequence, the contribution of this network tend to be the same as in the hard-backed layer case, cf. the absorption curves between Figs. 14(b) and 12. In particular, the absorption peak reappears at about 650 Hz, which is the quarter-wavelength resonance for this network. A rough plateau is formed between this and another absorption peak that occurs slightly below 800 Hz, see Fig. 14(b). The modelling correctly predicted this phenomenon, as well as the disappearance of the small peak (present in Case B at about 1.4 kHz) and the re-appearance of absorption peak near 2 kHz which is the three-quarter-wavelength resonance of network 1. The discrepancies between measurements and predictions are slightly larger at higher frequencies above 1.9 kHz, but the overall agreement is more than satisfactory. Especially, if we recall that network 1 is sealed with a relatively thin aluminium tape that can act as a septum that is not so perfectly rigid as assumed in the modelling.

Fig. 15 presents acoustic pressure distributions determined at 2200 kHz for each case study using the numerical MPEF model and DNS. At such a high frequency, the pressure distribution in each pore network is quite complex. When comparing the coloured contour maps of the real part of acoustic pressure, one should notice a great similarity in the pressure distribution (along the layer thickness) inside each pore network (DNS) and its corresponding EF domain (MPEF): in particular the pressure nodes are at the same position within the layer. Now, when the comparison is made between the pressure distribution in different pore networks (or,

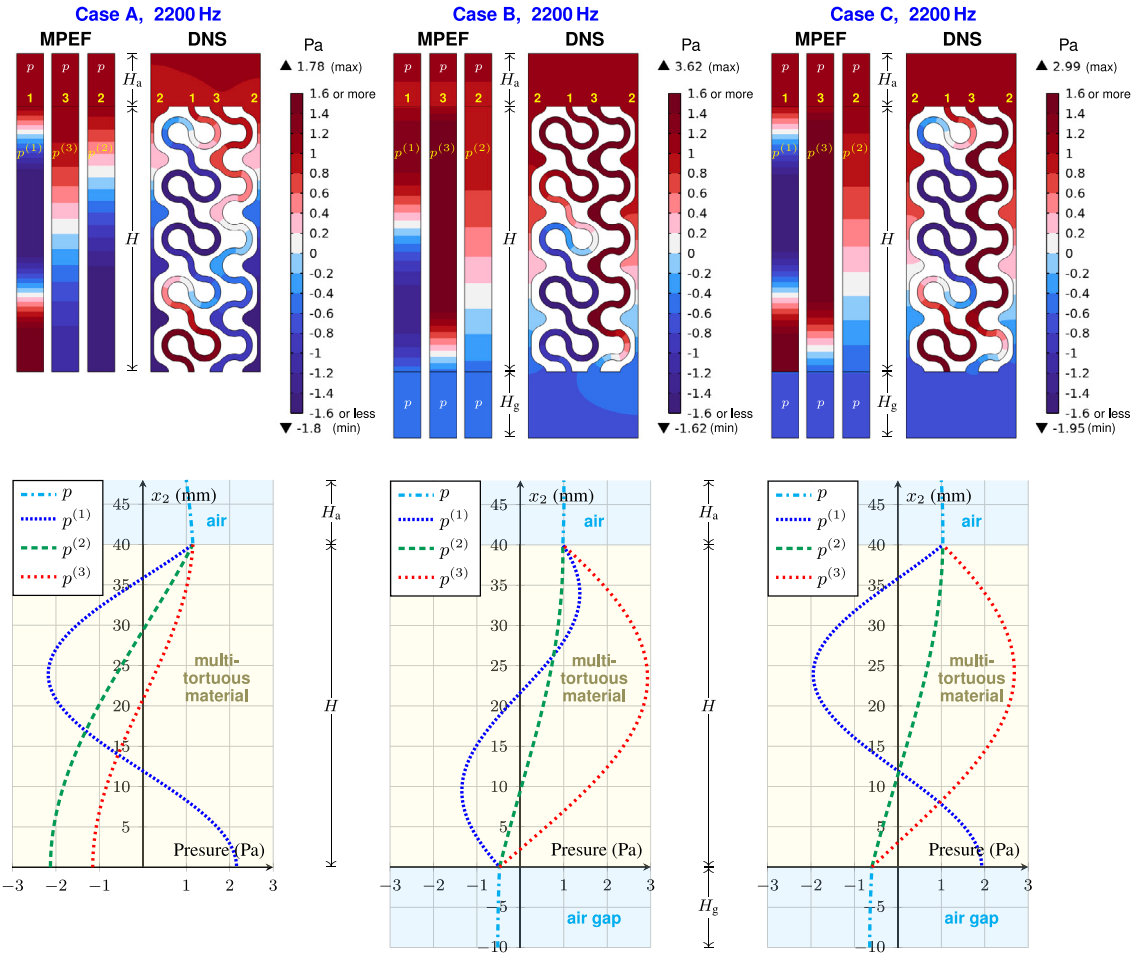

Fig. 15. Acoustic pressure (real part) distributions at 2200 Hz.

alternatively, in different EF domains), we can see that these distributions are very different and independent in Case A, especially between the pore network 1 (with two pressure nodes) and the pore network 2 or 3 (each with a single pressure node). When an air gap is added in Case B, the pressure distributions in each network and EF domain change significantly. In particular, there is only one pressure node in network 1 (EF 1). In Case C, the back entry to network 1 is sealed and the pressure distribution in this network again has two pressure nodes and is almost identical to Case A. This is evident when comparing the pressure distribution curves in each EF domain, produced using the MPEF method for each case study, see graphs in the lower row of Fig. 15. The pressure curves in EF 1 are almost identical for Cases A and C. Similarly, in Case B the pressure curves in EF 2 and EF 3 are very similar, although not identical, to their counterparts determined in Case C. It should also be noted that the pressures are equal between all EF domains at each interface with the air (or air gap) domain, and there is pressure continuity at these interfaces. Obviously, the pressure gradients are different for each EF, because the flow velocities (fluxes) coming from each network are different.

4.4. Atypical acoustic behaviour of multi-tortuous materials

In this section, we discuss in more detail the unusual acoustic behaviour — already reported above — of multi-tortuous materials, observed when a layer of such a multiple-network material is supported by an air gap. For this purpose, we compare in Fig. 16 how sound absorption changes when an air gap is introduced between the rear face of a porous layer and the rigid wall. We perform this comparison for three types of acoustic materials, namely:

1. a layer of glass wool as an example of a conventional acoustic treatment,
2. a single-network layer with network 1 defined by REV 1 shown in the upper left corner of Fig. 5(c), and
3. a multi-tortuous material layer with three separate networks 1, 2 and 3, as in REV 1+2+3 shown in the lower right corner of Fig. 5(c).

To make the comparison more meaningful, all layers have the same thickness of 40 mm. The conventional glass wool is also a single open-pore network material and was modelled as an equivalent fluid, see Appendix C for details and in particular Table C.1 for glass wool macro-parameters.

Fig. 16(a) compares the normal-incidence sound absorption curves calculated for the layer with network 1 with those calculated for the glass wool layer. In each case, three configurations were considered: (i) direct support by a rigid wall, and (ii) a 1 mm or (iii) a 10 mm air gap between the rigid wall and the back of the layer. For both materials, the well-known effect is observed when an air gap is introduced: all absorption peaks are shifted to lower frequencies. This is clearly visible for the layer with network 1, see Fig. 16(a): when a 1 mm air gap is introduced behind this layer, the quarter-wavelength resonance absorption peak is moved from position A to position B (at a frequency 80 Hz lower than A), and then to position C (located at only 300 Hz) when the air gap is increased to 10 mm. The change is very significant even with a gap of only 1 mm. Therefore, we strongly recommend sealing the back of a metamaterial sample with adhesive tape during impedance tube testing in a configuration with direct support on a rigid wall. Otherwise, measurement results may be distorted by the thin-gap effect, although theoretically, in the case of single-network materials, there is no distinction between the boundary perfectly bonded to the wall and the one with an *infinitely thin* air gap. This problem does not occur in the case of conventional acoustic materials, which are characterised by high porosity, low tortuosity, and much shorter characteristic lengths (see Table C.1 for typical glass wool parameters) compared to acoustic metamaterials with high tortuosity (see Table 1). All this results in broadband sound absorption: good in the mid-to-high frequency range, but poor at lower frequencies. Although the maximum absorption also corresponds to the quarter-wavelength resonance, absorption peaks are often not clearly visible, as in the case of the glass wool layer, see Fig. 16(a). As for all single-network materials, adding an air gap behind the fibrous layer shifts the resonance and absorption maximum to a lower frequency, e.g. from 2.7 kHz to 2.1 kHz when a 40 mm layer of glass wool is backed by a 10 mm air gap. However, for thinner air gaps (e.g. 1 mm thick) the effect is barely visible, see Fig. 16(a).

To understand how unusual the acoustic behaviour of the multi-tortuous material can be, the results shown in graph (a) of Fig. 16 should be confronted with those presented in graph (b). The latter were determined for the multi-tortuous layer in four configurations, because when such a layer is supported by a rigid wall, we can distinguish two cases, namely: (i) a perfectly sealing hard boundary (the SHB conditions), and (ii) a hard boundary with an infinitely thin air gap (the NCHB conditions). The remaining two configurations of the multi-tortuous layer backed by a finite-thickness air gap (1 mm or 10 mm thick) are the same as for single-network layers. The most dramatic change is observed between the first two cases, although both configurations are almost identical. However, when even an infinitely thin air gap appears at the back of the multi-tortuous layer, the first absorption peak is shifted to a *much higher* frequency: from position A′ at 650 Hz to position A″ at 1060 Hz, see Fig. 16(b). Moreover, the number of absorption peaks in the considered frequency range is reduced. This is because of the substantial difference between both boundary conditions. The perfect sealing conditions keep the networks separated (uncoupled) at the boundary, while the NCHB conditions equalise the pressure of all pore networks at the boundary, coupling them in this way. In this case, the networks are coupled on both sides of the porous layer. As a result, the multi-tortuous nature of the material is weakened, and consequently its multi-resonant behaviour. The NCHB condition is a direct predecessor of the interface conditions that couple the multi-tortuous material to an air domain, in particular to a finite-thickness air gap. Therefore, the two-layer configuration consisting of a multi-tortuous material backed by an air gap behaves in a more conventional manner as the air gap thickness is increased. Now, the absorption peaks are shifted to lower frequencies, e.g. the first peak from position A″ to B for a 1 mm air gap, and then to position C for a 10 mm air gap, see Fig. 16(b). However, the overall acoustic behaviour can still be considered anomalous since individual absorption peaks may be reduced due to the interaction of resonances and antiresonances associated with different networks.

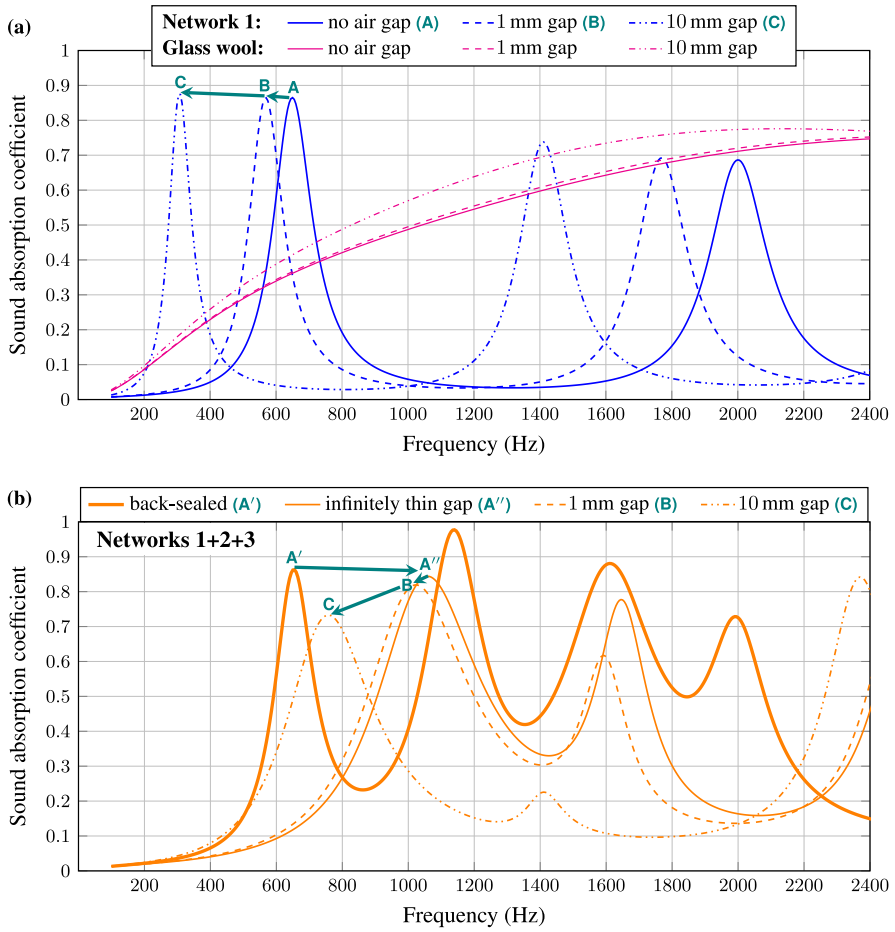

Fig. 16. Change in sound absorption due to the addition of an air gap at the back of the porous layer: (a) standard behaviour for a single-network material and a conventional acoustic material (glass wool), (b) atypical behaviour for a multi-tortuous material with separated pore networks. All porous layers have the same thickness of 40 mm.

5. Conclusions

We have proposed an original technique for designing multi-resonant acoustic materials with broadband efficiency. The technique is based on the informed design of tortuosity, which leads to the development of tailored multi-tortuous materials. These materials – especially when carefully designed – should exhibit extraordinary acoustic properties compared to conventional porous materials used in acoustic treatment. In particular, due to several separated networks with contrasting, high tortuosities, they allow for multiple quarter-wavelength resonances resulting in absorption peaks in the lower frequency range. On the other hand, they also exhibit atypical acoustic behaviour when backed by an air gap. This unusual behaviour distinguishes them significantly not only from conventional acoustic layers, but also from single-network materials (or even from materials with multiple pore networks of very similar tortuosities). This has been demonstrated using examples based on relatively simple two-dimensional designs.

Results obtained by semi-analytical modelling have been validated with two independent numerical methods, i.e. the numerical MPEF model and Navier–Stokes DNS, as well as with measurements from several experimental tests conducted on a 3D printed sample of the designed material. The experiments fully confirmed the occurrence of the multi-resonance phenomenon, as well as the unusual behaviour for configurations where the multi-tortuous layer is backed by an air gap.

The numerical MPEF model proposed in Section 2.2 is much more efficient than the computationally intensive Navier–Stokes DNS. It is also versatile compared to related semi-analytical calculations that are specified for one-dimensional problems of plane wave propagation at normal incidence. On the other hand, the procedure proposed in Section 3 is extremely effective because it is based on the semi-analytical calculations. It can be even fully analytical for specific pore network designs, such as constant-width tortuous channels, for which all necessary macro-parameters can be estimated analytically. We have demonstrated that this procedure allows for the very efficient and informed design of multi-tortuous acoustic materials. However, since the MPEF method is suitable for FE implementation, a homogenised multi-pressure model of the designed multi-tortuous material can be

easily implemented to analyse its effect in complex configurations that require FE calculations. Note that it is possible to implement design criteria other than impedance matching or desired sound absorption.

Regardless of the simple network shapes used in the 3D printed sample, MPEF modelling and the entire procedure for tortuosity-based design can be applied to materials with open porosity consisting of disconnected networks of almost any shape. Their micro-geometries can be very complex, combining different narrow or wider channels with variable and irregular cross-sections that connect cavities (pores) of different shapes and sizes, leading to significant visco-thermal dissipation of acoustic wave energy over a wider frequency range. Moreover, other dissipative phenomena in porous media modelled using equivalent fluids, such as pressure diffusion and sorption due to multi-scale porosity [55–57], local inner resonators [58], permeo-elastic effects [59], etc., can be taken into account provided that the viscous flows in different main pore networks are separated (e.g. *not* affected by the microporous skeleton), thereby preserving the multi-tortuous nature of the material.

To obtain the desired multi-resonant and possibly broadband behaviour, the pore networks in multi-tortuous materials must be tailored to have contrasting but also 'tuned' tortuosities. They must be kept apart but at the same time well fitted inside the material space so that the total porosity is as large as possible. Ways to achieve this goal are well illustrated through the two-dimensional benchmark examples presented in this work. Nevertheless, thin-layer designs of multi-tortuous materials that are particularly efficient in a wideband low-frequency range should rather be three-dimensional, such as systems of spatially twisted channels, nested networks and multi-periodic materials [60], etc.

CRediT authorship contribution statement

Tomasz G. Zieliński: Writing – original draft, Visualization, Software, Methodology, Investigation, Formal analysis, Conceptualization. **Marie-Annick Galland:** Writing – review & editing, Validation, Conceptualization.

Declaration of competing interest

The authors declare that they have no known competing financial interests or personal relationships that could have appeared to influence the work reported in this paper.

Acknowledgements

This research was financially supported by the National Science Centre (NCN), Poland, under Grant Agreement No. 2021/41/B/ST8/04492. It was also supported by the LABEX CeLyA (ANR-10-LABX-0060) of Université de Lyon, within the program "Investissements d'Avenir" (ANR-16-IDEX-0005) operated by the French National Research Agency (ANR).

Appendix A. Sound absorption coefficient

In all analyses of sound wave propagation, the sound absorption coefficient $\mathcal{A}$ was calculated at normal incidence from the reflection coefficient $\mathcal{R}$ as follows [1]

$$\mathcal{A}(\omega) = 1 - \left|\mathcal{R}(\omega)\right|^2, \qquad \mathcal{R}(\omega) = \frac{\mathcal{Z}_{\mathrm{S}}(\omega) - Z_{\mathrm{a}}}{\mathcal{Z}_{\mathrm{S}}(\omega) + Z_{\mathrm{a}}}. \tag{A.1}$$

Here, $\mathcal{Z}_{\mathrm{S}}(\omega)$ is the surface acoustic impedance of the sound-absorbing configuration, while Z_{a} is the characteristic impedance of the air in front of it. The sound absorption configurations considered in this work are: a porous layer set directly on a rigid wall, and a two-layer arrangement of a porous layer backed by an air gap. In all semi-analytical analyses, $\mathcal{Z}_{\mathrm{S}}$ was determined analytically as described in Section 2.1.2 for the single-network layers, and in Section 2.2.3 for the multiple-network layers. In all FE analyses, $\mathcal{Z}_{\mathrm{S}}$ was calculated as the ratio of the sound pressure to the particle velocity averaged over the boundary at a distance H_{a} above the porous layer, where waves become plane in Navier–Stokes simulations. This configuration has an additional air layer in front, and the surface acoustic impedance calculated here is different than that determined directly at the front of the porous layer (we determined them both in the case of Helmholtz-based MPEF analyses). However, the sound absorption coefficient is the same in both cases, since the propagation of sound in the air in front of the porous layer is lossless.

Appendix B. JCALP model

The frequency-dependent dynamic permeabilities for viscous and thermal effects, $\mathcal{K}_n$ and Θ_n, can be determined using the well-established JCALP model [41,46–48]. The essence of this model is the following scaling function

$$\Pi_\omega(\Pi_0, \mathcal{M}, \mathcal{P}, \omega_{\mathrm{c}}) = \Pi_0 \left(\frac{\mathrm{i}\omega}{\omega_{\mathrm{c}}} + 1 - \mathcal{P} + \sqrt{\mathcal{P}^2 + \frac{\mathcal{M}}{2}\frac{\mathrm{i}\omega}{\omega_{\mathrm{c}}}} \right)^{-1} \tag{B.1}$$

that depends on the static permeability Π_0 (i.e. the value of Π_ω at $\omega = 0$), two shape factors, $\mathcal{M}$ and $\mathcal{P}$, and a characteristic frequency ω_{c}. Those are calculated for visco-inertial and thermal effects as specified below, using eight macro-parameters given in Table 1. Therefore,

$$\mathcal{K}_n(\omega) = \Pi_\omega(\mathcal{K}_{0n}, \mathcal{M}_{\mathrm{v}n}, \mathcal{P}_{\mathrm{v}n}, \omega_{\mathrm{v}n}), \qquad \Theta_n(\omega) = \Pi_\omega(\Theta_0, \mathcal{M}_{\mathrm{t}n}, \mathcal{P}_{\mathrm{t}n}, \omega_{\mathrm{t}n}), \tag{B.2}$$

Table C.1
JCAL parameters for glass wool [61].

ϕ_{w} %	$\alpha_{\infty\mathrm{w}}$ –	Λ_{vw} mm	Λ_{tw} mm	$\mathcal{K}_{0\mathrm{w}}$ 10^{-9} m^2	$\Theta_{0\mathrm{w}}$ 10^{-9} m^2
98.6	1.01	0.225	0.388	4.64	6.30

where the viscous and thermal shape factors are

$$\mathcal{M}_{\mathrm{v}n}=\frac{8\mathcal{K}_{0n}\alpha_{\infty n}}{\phi_n\Lambda_{\mathrm{v}n}^2}\,,\quad \mathcal{P}_{\mathrm{v}n}=\frac{\mathcal{M}_{\mathrm{v}n}}{4(\alpha_{0\mathrm{v}n}/\alpha_{\infty n}-1)}\,,\qquad \mathcal{M}_{\mathrm{t}n}=\frac{8\Theta_{0n}}{\phi_n\Lambda_{\mathrm{t}n}^2}\,,\quad \mathcal{P}_{\mathrm{t}n}=\frac{\mathcal{M}_{\mathrm{t}n}}{4(\alpha_{0\mathrm{t}}-1)}\,. \tag{B.3}$$

The corresponding viscous and thermal characteristic frequencies, i.e.

$$\omega_{\mathrm{v}n}=\frac{\phi_n\nu_{\mathrm{a}}}{\mathcal{K}_{0n}\alpha_{\infty n}}\,,\qquad \omega_{\mathrm{t}n}=\frac{\phi_n\tau_{\mathrm{a}}}{\Theta_{0n}}\,, \tag{B.4}$$

additionally depend on the kinematic viscosity ν_{a} and thermal diffusivity τ_{a} of the air saturating the pore network.

Appendix C. Glass wool macro-parameters and JCAL model

The Johnson–Champoux–Allard–Lafarge (JCAL) model [41,46,47] was used to calculate the dynamic viscous and thermal permeabilities, $\mathcal{K}_{\mathrm{w}}$ and Θ_{w}, for glass wool. The JCAL model is a reduced version of the JCALP model (B.1) with $\mathcal{P}=1$. Therefore,

$$\mathcal{K}_{\mathrm{w}}(\omega)=\Pi_{\omega}(\mathcal{K}_{0\mathrm{w}},\mathcal{M}_{\mathrm{vw}},1,\omega_{\mathrm{vw}})\,,\qquad \Theta_{\mathrm{w}}(\omega)=\Pi_{\omega}(\Theta_{0\mathrm{w}},\mathcal{M}_{\mathrm{tw}},1,\omega_{\mathrm{tw}})\,, \tag{C.1}$$

where the required viscous and thermal shape factors and characteristic frequencies, i.e.

$$\mathcal{M}_{\mathrm{vw}}=\frac{8\mathcal{K}_{0\mathrm{w}}\alpha_{\infty\mathrm{w}}}{\phi_{\mathrm{w}}\Lambda_{\mathrm{vw}}^2}\,,\quad \mathcal{M}_{\mathrm{tw}}=\frac{8\Theta_{0\mathrm{w}}}{\phi_{\mathrm{w}}\Lambda_{\mathrm{tw}}^2}\,,\qquad \omega_{\mathrm{vw}}=\frac{\phi_{\mathrm{w}}\nu_{\mathrm{a}}}{\mathcal{K}_{0\mathrm{w}}\alpha_{\infty\mathrm{w}}}\,,\quad \omega_{\mathrm{tw}}=\frac{\phi_{\mathrm{w}}\tau_{\mathrm{a}}}{\Theta_{0\mathrm{w}}}\,, \tag{C.2}$$

depend on six macro-parameters: the glass wool porosity ϕ_{w}, tortuosity $\alpha_{\infty\mathrm{w}}$, characteristic lengths, Λ_{vw} and Λ_{tw}, and static permeabilities, $\mathcal{K}_{0\mathrm{w}}$ and $\Theta_{0\mathrm{w}}$. Their values are given in Table C.1. The dynamic permeabilities (C.1) calculated for glass wool, as well as its porosity ϕ_{w}, were used to determine the effective properties of the corresponding EF, using formulas (2) and (5), after formally replacing 'n' with 'w'.

Data availability

Data will be made available on request.

References

[1] J.F. Allard, N. Atalla, Propagation of Sound in Porous Media: Modeling Sound Absorbing Materials, second ed., John Wiley & Sons, Chichester, 2009, http://dx.doi.org/10.1002/9780470747339.

[2] J.-P. Groby, N. Jiménez, V. Romero-García, Acoustic metamaterial absorbers, in: J.-P. Groby N. Jiménez (Ed.), Acoustic Waves in Periodic Structures, Metamaterials, and Porous Media: From Fundamentals to Industrial Applications, Springer International Publishing, Cham, 2021, pp. 167–204, http://dx.doi.org/10.1007/978-3-030-84300-7_5, (Chapter 5).

[3] X. Cai, Q. Guo, G. Hu, J. Yang, Ultrathin low frequency sound absorbing panels based on coplanar spiral tubes or coplanar Helmholtz resonators, Appl. Phys. Lett. 105 (2014) 121901, http://dx.doi.org/10.1063/1.4895617.

[4] Y. Li, B.M. Assouar, Acoustic metasurface-based perfect absorber with deep subwavelength thickness, Appl. Phys. Lett. 108 (2016) 063502, http://dx.doi.org/10.1063/1.4941338.

[5] Y. Wang, H. Zhao, H. Yang, J. Zhong, D. Zhao, Z. Lu, J. Wen, A tunable sound-absorbing metamaterial based on coiled-up space, J. Appl. Phys. 123 (2018) 185109, http://dx.doi.org/10.1063/1.5026022.

[6] J.-S. Chen, Y.-B. Chen, Y.-H. Cheng, L.-C. Chou, A sound absorption panel containing coiled Helmholtz resonators, Phys. Lett. A 384 (35) (2020) 126887, http://dx.doi.org/10.1016/j.physleta.2020.126887.

[7] K. Donda, Y. Zhu, S.-W. Fan, L. Cao, Y. Li, B. Assouar, Extreme low-frequency ultrathin acoustic absorbing metasurface, Appl. Phys. Lett. 115 (2019) 173506, http://dx.doi.org/10.1063/1.5122704.

[8] S. Kumar, H.P. Lee, Labyrinthine acoustic metastructures enabling broadband sound absorption and ventilation, Appl. Phys. Lett. 116 (2020) 134103, http://dx.doi.org/10.1063/5.0004520.

[9] T. Yuan, X. Song, J. Xu, B. Pan, D. Sui, H. Xiao, J. Zhou, Tunable acoustic composite metasurface based porous material for broadband sound absorption, Compos. Struct. 298 (2022) 116014, http://dx.doi.org/10.1016/j.compstruct.2022.116014.

[10] T.G. Zieliński, K.C. Opiela, N. Dauchez, T. Boutin, M.-A. Galland, K. Attenborough, Extremely tortuous sound absorbers with labyrinthine channels in non-porous and microporous solid skeletons, Appl. Acoust. 217 (2024) 109816, http://dx.doi.org/10.1016/j.apacoust.2023.109816.

[11] F. De Bie, H. Denayer, E. Deckers, Derivation, verification and validation of a length correction factor for folded quarter-wavelength resonators, Acta Acust. 9 (2025) 38, http://dx.doi.org/10.1051/aacus/2025022.

[12] G. Catapane, G. Petrone, O. Robin, K. Verdière, Coiled quarter wavelength resonators for low-frequency sound absorption under plane wave and diffuse acoustic field excitations, Appl. Acoust. 209 (2023) 109402, http://dx.doi.org/10.1016/j.apacoust.2023.109402.

[13] D. Ramos, L. Godinho, P. Amado-Mendes, P. Mareze, Broadband low-frequency bidimensional honeycomb lattice metastructure based on the coupling of subwavelength resonators, Appl. Acoust. 199 (2022) 109038, http://dx.doi.org/10.1016/j.apacoust.2022.109038.
[14] D. Ramos, F. Pompoli, C. Marescotti, L. Godinho, P. Amado-Mendes, P. Mareze, Modelling the effective sound propagation properties of a hexagonal acoustic metamaterial using a dissipative equivalent-fluid approach under different termination conditions, J. Sound Vib. 598 (2025) 118855, http://dx.doi.org/10.1016/j.jsv.2024.118855.
[15] K. Sakagami, Y. Nagayama, M. Morimoto, M. Yairi, Pilot study on wideband sound absorber obtained by combination of two different microperforated panel (MPP) absorbers, Acoust. Sci. Technol. 30 (2) (2009) 154–156, http://dx.doi.org/10.1250/ast.30.154.
[16] M. Yairi, K. Sakagami, K. Takebayashi, M. Morimoto, Excess sound absorption at normal incidence by two microperforated panel absorbers with different impedance, Acoust. Sci. Technol. 32 (5) (2011) 194–200, http://dx.doi.org/10.1250/ast.32.194.
[17] F. Chevillotte, Controlling sound absorption by an upstream resistive layer, Appl. Acoust. 73 (1) (2012) 56–60, http://dx.doi.org/10.1016/j.apacoust.2011.07.005.
[18] C. Wang, L. Huang, Y. Zhang, Oblique incidence sound absorption of parallel arrangement of multiple micro-perforated panel absorbers in a periodic pattern, J. Sound Vib. 333 (25) (2014) 6828–6842, http://dx.doi.org/10.1016/j.jsv.2014.08.009.
[19] K. Verdière, R. Panneton, S. Elkoun, T. Dupont, P. Leclaire, Transfer matrix method applied to the parallel assembly of sound absorbing materials, J. Acoust. Soc. Am. 134 (6) (2013) 4648–4658, http://dx.doi.org/10.1121/1.4824839.
[20] D. Li, D. Chang, B. Liu, Enhanced low- to mid-frequency sound absorption using parallel-arranged perforated plates with extended tubes and porous material, Appl. Acoust. 127 (2017) 316–323, http://dx.doi.org/10.1016/j.apacoust.2017.06.019.
[21] H.-S. Kim, P.-S. Ma, B.-K. Kim, S.-R. Kim, S.-H. Lee, Low-frequency sound absorption of elastic micro-perforated plates in a parallel arrangement, J. Sound Vib. 460 (2019) 114884, http://dx.doi.org/10.1016/j.jsv.2019.114884.
[22] G. do N. Almeida, E.F. Vergara, L.R. Barbosa, R. Brum, Low-frequency sound absorption of a metamaterial with symmetrical-coiled-up spaces, Appl. Acoust. 172 (2021) 107593, http://dx.doi.org/10.1016/j.apacoust.2020.107593.
[23] Y. Liu, X. Zeng, S. Ren, W. Sun, H. Wang, Y. Lei, A broadband multi-resonant sound-absorbing metastructure based on impedance-matching nesting channels, Appl. Acoust. 223 (2024) 110099, http://dx.doi.org/10.1016/j.apacoust.2024.110099.
[24] N. Katiyar, S.S. Choudhury, V.D. Mishra, S. Bhattacharya, Broadband low-to-mid-range frequency sound absorption using a micro-perforated panel with variable-depth parallel u-shaped cavities, J. Appl. Phys. 137 (10) (2025) 103102, http://dx.doi.org/10.1063/5.0240804.
[25] H. Min, H. Lou, Y. Zhao, Optimization of parallel coiled cavities of different depths in microperforated panel sound absorbers, Sci. Rep. 15 (2025) 1401, http://dx.doi.org/10.1038/s41598-025-85171-3.
[26] A. Magnani, C. Marescotti, F. Pompoli, Acoustic absorption modeling of single and multiple coiled-up resonators, Appl. Acoust. 186 (2022) 108504, http://dx.doi.org/10.1016/j.apacoust.2021.108504.
[27] A. Carvalho de Sousa, E. Deckers, C. Claeys, W. Desmet, On the assembly of Archimedean spiral cavities for sound absorption applications: Design, optimization and experimental validation, Mech. Syst. Signal Process. 147 (2021) 107102, http://dx.doi.org/10.1016/j.ymssp.2020.107102.
[28] X. Yang, X. Shen, F. Yang, Z. Yin, F. Yang, Q. Yang, C. Shen, M. Xu, J. Wan, Acoustic metamaterials of modular nested Helmholtz resonators with multiple tunable absorption peaks, Appl. Acoust. 213 (2023) 109647, http://dx.doi.org/10.1016/j.apacoust.2023.109647.
[29] Z. Mei, Y. Lyu, X. Li, X. Cheng, J. Yang, Parallel-coupled hierarchical and reconfigurable structure for broadband sound absorption, Appl. Acoust. 221 (2024) 109990, http://dx.doi.org/10.1016/j.apacoust.2024.109990.
[30] N. Jiménez, V. Romero-García, V. Pagneux, J.-P. Groby, Rainbow-trapping absorbers: Broadband, perfect and asymmetric sound absorption by subwavelength panels for transmission problems, Sci. Rep. 7 (1) (2017) http://dx.doi.org/10.1038/s41598-017-13706-4.
[31] A. Jamois, D. Dragna, T.G. Zieliński, M.-A. Galland, Acoustic absorption of 3D printed samples at normal incidence and as a duct liner, Acta Acust. 9 (2025) 12, http://dx.doi.org/10.1051/aacus/2024088.
[32] J. Boulvert, G. Gabard, V. Romero-García, J.-P. Groby, Compact resonant systems for perfect and broadband sound absorption in wide waveguides in transmission problems, Sci. Rep. 12 (2022) 10013, http://dx.doi.org/10.1038/s41598-022-13944-1.
[33] H. Wang, X. Zeng, S. Ren, D. Xue, Z. Li, H. Wang, Y. Lei, Low-frequency sound attenuation by coiled-up meta-liner with nonuniform cross sections under grazing flow, J. Appl. Phys. 135 (20) (2024) 203107, http://dx.doi.org/10.1063/5.0203941.
[34] T. Bravo, C. Maury, Converging rainbow trapping silencers for broadband sound dissipation in a low-speed ducted flow, J. Sound Vib. 589 (2024) 118524, http://dx.doi.org/10.1016/j.jsv.2024.118524.
[35] P. Leclaire, O. Umnova, T. Dupont, R. Panneton, Acoustical properties of air-saturated porous material with periodically distributed dead-end pores, J. Acoust. Soc. Am. 137 (4) (2015) 1772–1782, http://dx.doi.org/10.1121/1.4916712.
[36] G. Bezançon, O. Doutres, O. Umnova, P. Leclaire, T. Dupont, Thin metamaterial using acoustic black hole profiles for broadband sound absorption, Appl. Acoust. 216 (2024) 109744, http://dx.doi.org/10.1016/j.apacoust.2023.109744.
[37] M. Červenka, M. Bednařík, Numerical study of the behavior of rectangular acoustic black holes for sound absorption in air, Wave Motion 123 (2023) 103230, http://dx.doi.org/10.1016/j.wavemoti.2023.103230.
[38] E. Sanchez-Palencia, Non-Homogenous Media and Vibration Theory, in: Lecture Notes in Physics, Springer-Verlag, 1980, http://dx.doi.org/10.1007/3-540-10000-8.
[39] J.-L. Auriault, C. Boutin, C. Geindreau, Homogenization of Coupled Phenomena in Heterogenous Media, ISTE Ltd. John Wiley & Sons, Inc, 2009, http://dx.doi.org/10.1002/9780470612033.
[40] T.G. Zieliński, R. Venegas, C. Perrot, M. Červenka, F. Chevillotte, K. Attenborough, Benchmarks for microstructure-based modelling of sound absorbing rigid-frame porous media, J. Sound Vib. 483 (2020) 115441, http://dx.doi.org/10.1016/j.jsv.2020.115441.
[41] D.L. Johnson, J. Koplik, R. Dashen, Theory of dynamic permeability and tortuosity in fluid-saturated porous media, J. Fluid Mech. 176 (1987) 379–402, http://dx.doi.org/10.1017/S0022112087000727.
[42] N. Jiménez, J.-P. Groby, V. Romero-García, The transfer matrix method in acoustics, in: N. Jiménez, O. Umnova, J.-P. Groby (Eds.), Acoustic Waves in Periodic Structures, Metamaterials, and Porous Media: From Fundamentals to Industrial Applications, Springer International Publishing, Cham, 2021, pp. 103–164, http://dx.doi.org/10.1007/978-3-030-84300-7_4, (Chapter 4).
[43] A. Dell, A. Krynkin, K. Horoshenkov, The use of the transfer matrix method to predict the effective fluid properties of acoustical systems, Appl. Acoust. 182 (2021) 108259, http://dx.doi.org/10.1016/j.apacoust.2021.108259.
[44] K. Verdière, R. Panneton, S. Elkoun, T. Dupont, P. Leclaire, Comparison between parallel transfer matrix method and admittance sum method, J. Acoust. Soc. Am. 136 (2) (2014) EL90–EL95, http://dx.doi.org/10.1121/1.4885481.
[45] K. Attenborough, Microstructures for lowering the quarter wavelength resonance frequency of a hard-backed rigid-porous layer, Appl. Acoust. 130 (2018) 188–194, http://dx.doi.org/10.1016/j.apacoust.2017.09.022.
[46] Y. Champoux, J.-F. Allard, Dynamic tortuosity and bulk modulus in air-saturated porous media, J. Appl. Phys. 70 (1991) 1975–1979, http://dx.doi.org/10.1063/1.349482.
[47] D. Lafarge, P. Lemarinier, J.F. Allard, V. Tarnow, Dynamic compressibility of air in porous structures at audible frequencies, J. Acoust. Soc. Am. 102 (4) (1997) 1995–2006, http://dx.doi.org/10.1121/1.419690.
[48] S.R. Pride, F.D. Morgan, A.F. Gangi, Drag forces of porous-medium acoustics, Phys. Rev. B 47 (9) (1993) 4964–4978, http://dx.doi.org/10.1103/PhysRevB.47.4964.

[49] C. Perrot, F. Chevillotte, R. Panneton, Bottom-up approach for microstructure optimization of sound absorbing materials, J. Acoust. Soc. Am. 124 (2) (2008) 940–948, http://dx.doi.org/10.1121/1.2945115.
[50] C.-Y. Lee, M.J. Leamy, J.H. Nadler, Acoustic absorption calculation in irreducible porous media: A unified computational approach, J. Acoust. Soc. Am. 126 (4) (2009) 1862–1870, http://dx.doi.org/10.1121/1.3205399.
[51] B. Ghanbarian, A.G. Hunt, R.P. Ewing, M. Sahimi, Tortuosity in porous media: A critical review, Soil Sci. Am. J. 77 (5) (2013) 1461–1477, http://dx.doi.org/10.2136/sssaj2012.0435.
[52] ISO 10534-2: Determination of sound absorption coefficient and impedance in impedance tubes, 1998.
[53] A. Jamois, D. Dragna, M.-A. Galland, Impact of leakage on sound properties of 3D printed samples at normal and grazing incidence, J. Acoust. Soc. Am. 158 (1) (2025) 75–83, http://dx.doi.org/10.1121/10.0037074.
[54] F. Marchetti, F. Chevillotte, On the modeling of imperfect interfaces in multilayers with transfer matrix method, J. Sound Vib. 600 (2025) 118898, http://dx.doi.org/10.1016/j.jsv.2024.118898.
[55] X. Olny, C. Boutin, Acoustic wave propagation in double porosity media, J. Acoust. Soc. Am. 114 (2003) 73–89, http://dx.doi.org/10.1121/1.1534607.
[56] R. Venegas, C. Boutin, Acoustics of sorptive porous materials, Wave Motion 68 (2017) 162–181, http://dx.doi.org/10.1016/j.wavemoti.2016.09.010.
[57] T.G. Zieliński, N. Dauchez, T. Boutin, M. Leturia, A. Wilkinson, F. Chevillotte, F.-X. Bécot, R. Venegas, Taking advantage of a 3D printing imperfection in the development of sound-absorbing materials, Appl. Acoust. 197 (2022) 108941, http://dx.doi.org/10.1016/j.apacoust.2022.108941.
[58] C. Boutin, Acoustics of porous media with inner resonators, J. Acoust. Soc. Am. 134 (6) (2013) 4717–4729, http://dx.doi.org/10.1121/1.4824965.
[59] R. Venegas, C. Boutin, Acoustics of permeo-elastic materials, J. Fluid Mech. 828 (2017) 135–174, http://dx.doi.org/10.1017/jfm.2017.505.
[60] X. Guan, E. Deckers, H. Dong, M. Hornikx, J. Yang, Optimization of graded porous acoustic absorbers based on triply periodic minimal surfaces, Mater. Des. 253 (2025) 113852, http://dx.doi.org/10.1016/j.matdes.2025.113852.
[61] L. Lei, N. Dauchez, J. Chazot, Prediction of the six parameters of an equivalent fluid model for thermocompressed glass wools and melamine foam, Appl. Acoust. 139 (2018) 44–56, http://dx.doi.org/10.1016/j.apacoust.2018.04.010.